

Tracing the Intrinsic Shapes of Dwarf Galaxies out to Four Effective Radii: Clues to Low-Mass Stellar Halo Formation

ERIN KADO-FONG,¹ JENNY E. GREENE,¹ SONG HUANG,¹ RACHAEL BEATON,^{1,2,*} ANDY D. GOULDING,¹ AND YUTAKA KOMIYAMA^{3,4}

¹*Department of Astrophysical Sciences, Princeton University, Princeton, NJ 08544, USA*

²*The Observatories of the Carnegie Institution for Science, 813 Santa Barbara Street, Pasadena, CA 91101, USA*

³*National Astronomical Observatory of Japan, 2-21-1 Osawa, Mitaka, Tokyo 181-8588, Japan*

⁴*Graduate University for Advanced Studies (SOKENDAI), 2-21-1 Osawa, Mitaka, Tokyo 181-8588, Japan*

(Dated: July 22, 2020)

ABSTRACT

Though smooth, extended spheroidal stellar outskirts have long been observed around nearby dwarf galaxies, it is unclear whether dwarfs generically host an extended stellar halo. We use imaging from the Hyper Suprime-Cam Subaru Strategic Program (HSC-SSP) to measure the shapes of dwarf galaxies out to four effective radii for a sample of dwarfs at $0.005 < z < 0.2$ and $10^{7.0} < M_{\star}/M_{\odot} < 10^{9.6}$. We find that dwarfs are slightly triaxial, with a $\langle B/A \rangle \gtrsim 0.75$ (where the ellipsoid is characterized by three principle semi-axes constrained by $C \leq B \leq A$). At $M_{\star} > 10^{8.5} M_{\odot}$, the galaxies grow from thick disk-like near their centers towards the spheroidal extreme at four effective radii. We also see that although blue dwarfs are, on average, characterized by thinner discs than red dwarfs, both blue and red dwarfs grow more spheroidal as a function of radius. This relation also holds true for a comparison between field and satellite dwarfs. This uniform trend towards relatively spheroidal shapes as a function of radius is consistent with an in-situ formation mechanism for stellar outskirts around low-mass galaxies, in agreement with proposed models where star formation feedback produces round stellar outskirts around dwarfs.

1. INTRODUCTION

The existence of a smooth stellar component in the outskirts of local dwarfs is a common, but puzzling, phenomenon (Lin & Faber 1983; Minniti & Zijlstra 1996; Grebel 1999; Minniti et al. 1999; Roychowdhury et al. 2013). Round stellar halos are a near-ubiquitous component of more massive galaxies – thought to be assembled largely through the accretion of satellite galaxies, the stars that populate these outskirts provide key insights into the galaxy’s assembly history (see, e.g. Bullock & Johnston 2005; Abadi et al. 2006). Due to a decreasing stellar mass to halo mass ratio, satellite accretion by dwarf centrals deposits fewer stars per unit halo mass than analogous events around more massive systems (Purcell et al. 2007; Brook et al. 2014). It is thus considered unlikely that minor mergers are able to fuel the formation of a stellar halo in dwarf galaxies.

Instead, it has been suggested that the stellar outskirts of dwarfs are an in-situ structure. In the field, dwarf galaxies sit in shallow potential wells; their structure is therefore more sensitive to the details of star formation feedback than more massive galaxies. Supernovae-driven winds (Hu 2019), cosmic ray feedback (Dashyan & Dubois 2020), stellar winds, radiation pressure, and photoionization (El-Badry et al. 2016) are all expected to more efficiently displace gas in dwarfs than in more massive hosts (both in moving gas to large radii and in removing it from the system entirely). In particular, hydrodynamical simulations have predicted that star formation feedback can induce significant size fluctuations in the stellar content of dwarf galaxies, driving the formation of a round stellar halo by inducing radial migration via potential fluctuations, as well as forming stars in outflowing and inflowing gas (Stinson et al. 2009; Maxwell et al. 2012; El-Badry et al. 2016).

Not all theories of dwarf stellar halo formation are purely in-situ, however; Bekki (2008) suggested that round stellar outskirts around dwarfs may be formed as a product of dwarf-dwarf major mergers (a merger

Corresponding author: Erin Kado-Fong
kadofong@princeton.edu

* Hubble Fellow

wherein the mass of the secondary is at most a factor of ~ 3 less than that of the primary). Such major mergers are expected to occur for about 75% of galaxies in this stellar mass range, but are expected to proceed far more often in the early universe – only 30% of these galaxies are expected to have undergone a major merger in the last 10 Gyr (Deason et al. 2014; Besla et al. 2018). Stellar outskirts formed in this manner would tend to be comprised of ancient stellar populations; using the surface brightness profile given by Bekki (2008) directly after the outskirts are formed and taking into account surface brightness dimming due to passive evolution (Conroy et al. 2009), in the major merger scenario we would not expect to detect an extended round stellar component around the majority of dwarfs.

Moreover, the dwarfs that have been found to host extended, smooth intermediate-old age stellar populations are nearby systems in the Local Volume (and mostly in the Local Group, see Zaritsky et al. 2000; Aparicio & Tikhonov 2000; Aparicio et al. 2000; Hidalgo et al. 2003; Demers et al. 2006; Bernard et al. 2007; Stinson et al. 2009; Strader et al. 2012; Nidever et al. 2019a,b; Pucha et al. 2019). It remains unclear whether such a structure is a generic feature of dwarfs (pointing to an in-situ origin), or a result of the influence of the more massive galaxies in the Local Group.

Understanding the intrinsic shape of dwarf galaxies is thus of interest in understanding the stellar assembly of these low-mass systems, and for constraining recipes for star formation feedback. However, it has historically been challenging to construct a sample of dwarfs with sufficient numbers whose imaging is deep enough to measure stable ellipticity profiles. Previous works have been confined to the Local Volume (Roychowdhury et al. 2013), or to the most massive dwarfs ($M_\star > 10^9 M_\odot$, Padilla & Strauss 2008; van der Wel et al. 2014; Zhang et al. 2019). Moreover, there has not been an effort previously to measure the intrinsic shapes of dwarf outskirts, due largely to the aforementioned technical hurdles.

In this work, we combine the large sample of spectroscopically confirmed dwarfs observed by the Sloan Digital Sky Survey spectroscopic surveys (both legacy and BOSS surveys, Strauss et al. 2002; Dawson et al. 2013; Reid et al. 2016) and the Galaxy and Mass Assembly (GAMA) spectroscopic survey (Baldry et al. 2012) with the wide and deep imaging of the Hyper Suprime-Cam Subaru Strategic Program (HSC-SSP; Aihara et al. 2018a,b; Miyazaki et al. 2018; Komiyama et al. 2018; Kawanomoto et al. 2018; Furusawa et al. 2018; Bosch et al. 2018; Huang et al. 2018b; Coupon et al. 2018) to

quantify the 3D shape distribution of dwarf galaxies as a function of radius.

The wide area covered by the HSC-SSP in conjunction with the surface brightness sensitivity and high resolution of its imaging allows us to map stable ellipticity profiles of the dwarfs out to four times the half-light radius ($R = 4R_{\text{eff}}$, where R_{eff} is defined by a single Sérsic fit, as described in Section 3) at $0.005 < z < 0.2$ and $7.0 \leq \log_{10}(M_\star/M_\odot) \leq 9.6$. This allows us to construct a sufficiently large sample of dwarfs to infer the distribution of their intrinsic shapes from observations of their projected 2D shapes at fixed radius. In Section 2, we detail the sample selection and volume corrections implemented for the sample. We detail the methodology and validation of the 1D surface brightness profiles and the 3D shape inference separately, in Section 3 and Section 4, respectively. We then examine the change in dwarf 3D shape as a function of radius and dwarf properties in Section 5, and consider the implications of the observed shape evolution to proposed dwarf stellar halo formation mechanisms in Section 6.

Throughout this paper we adopt a standard flat Λ CDM model in which $H_0 = 70 \text{ km s}^{-1} \text{ Mpc}^{-1}$ and $\Omega_m = 0.3$.

2. OBSERVATIONS AND DATA PROCESSING

2.1. HSC-SSP Imaging

As noted above, the HSC-SSP imaging boasts wide, deep, and high resolution imaging, making it well-suited for an exploration of the low surface brightness outskirts of low-mass galaxies. Upon completion, HSC-SSP will provide imaging with a median seeing of $\sim 0.6''$ in the i_{HSC} over ~ 1400 square degrees to a point source depth of $i_{\text{HSC}} \sim 26$ in its shallowest “Wide” layer (Aihara et al. 2019). The data have been shown to reach surface brightness limits of $i_{\text{HSC}} \sim 28.5 \text{ mag arcsec}^{-2}$ for measurements around a known target (Huang et al. 2018a). We test the surface brightness limit of the HSC-SSP data in the vicinity of our sample in Appendix A, and find that $\mu_i = 28.5 \text{ mag arcsec}^{-2}$ is a conservative choice of limiting surface brightness. Indeed, with an empirical correction to the background, it has been shown that HSC-SSP reaches depths of $\mu_r \sim 29.5 \text{ mag arcsec}^{-2}$. However, because we allow several parameters to drift during our surface brightness profile measurements, we adopt the fiducial surface brightness limit of $\mu_i = 28.5 \text{ mag arcsec}^{-2}$.

For this work, we use the internal HSC-SSP S18A data release, which covers the same area as the second public data release of Aihara et al. (2019) and is processed with a very similar data reduction pipeline. Though there are some minor differences between the data reduction

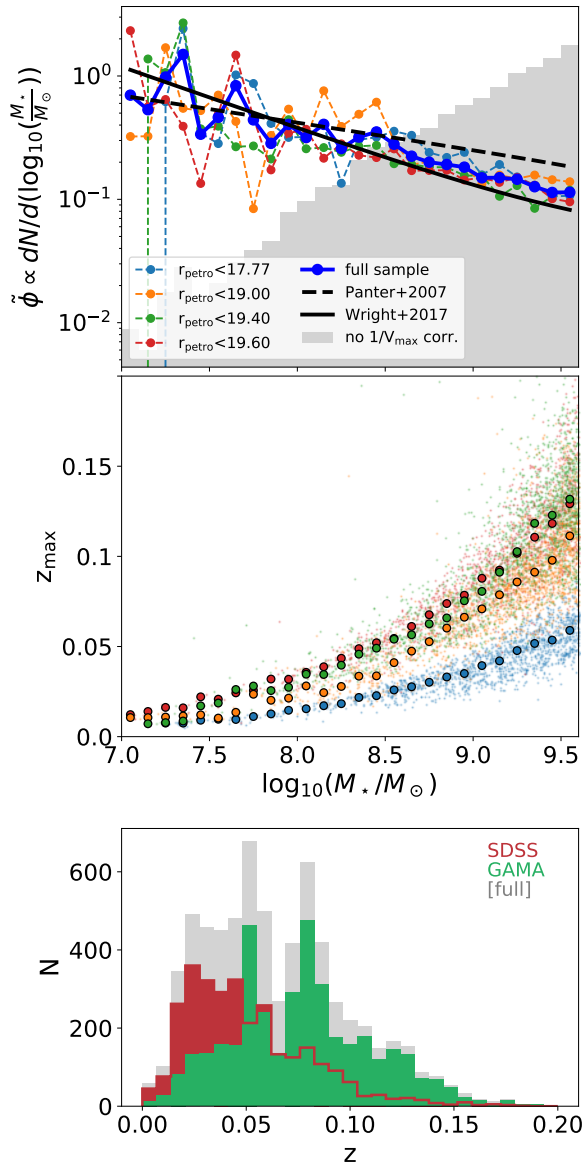


Figure 1. *Top:* we show the normalized stellar mass function (SMF), $\tilde{\phi}(\log_{10}(M_*/M_\odot))$, for each magnitude-limited subset of our sample with dash-connected scatter. The normalized SMF for the full sample is shown by the solid blue curve. For reference, the Schechter fit of Panter et al. (2007) and the double Schechter fit of Wright et al. (2017) are normalized to our stellar mass range and shown in the dashed and solid lines, respectively. The raw distribution in stellar mass (i.e. without $1/V_{\text{max}}$ weights) is shown by the grey filled histogram. We find that our normalized SMF matches that of Wright et al. (2017) well. *Middle:* the maximum observable redshift, z_{max} , for each galaxy in the sample as a function of stellar mass. As at top, points are colored by the magnitude limit of the source spectroscopic program. The mean z_{max} as a function of stellar mass is also shown for each program by the large scatter points. *Bottom:* the redshift distribution, colored by source survey.

pipeline used for S18A and PDR2, these changes do not affect the parts of the pipeline discussed in this work. We require only coverage in the i_{HSC} band, resulting in an area of $\sim 796 \text{ deg}^2$ with a point source depth of $i = 26.2^{+0.2}_{-0.4}$. The i_{HSC} band is best choice to study the overall shape of the stellar distribution for two main reasons. First, the i_{HSC} bands has best seeing out of the five HSC bands. Second, it is less sensitive to dust extinction and star forming regions relative to the bluer g_{HSC} and r_{HSC} bands, and deeper than the redder z_{HSC} and y_{HSC} are significantly shallower.

2.2. Initial Sample Selection

All dwarfs in the present sample have been spectroscopically observed by either the SDSS or GAMA spectroscopic surveys. We limit our sample to dwarfs at $0.005 < z < 0.2$; the redshift distribution of the sample peaks at $z \lesssim 0.05$, as shown in the bottom panel of Figure 1. Due to the intrinsic faintness of low-mass galaxies, the majority of our sample is at $z \lesssim 0.1$.

This selection yields a sample of 11338 dwarfs. In 3128 cases, there is a bright star (or related imaging artifact) within $5R_{\text{eff}}$ of the target galaxy; because our goal is to measure ellipticity profiles out to the outskirts of the dwarfs, we remove these galaxies from the final sample. An additional 548 galaxies are too close to neighbors to measure a reliable surface brightness profile, or are coincident with an imaging artifact.

We adopt stellar masses measured by the SDSS and GAMA teams. The stellar masses measured by the GAMA team use a Chabrier initial mass function (Chabrier 2003) by Taylor et al. (2011). The stellar masses measured by the SDSS team are derived using the Conroy et al. (2009) Flexible Stellar Population Synthesis (FSPS) models with a Kroupa initial mass function (Kroupa 2001). In Kado-Fong et al. (2020), we found that, for galaxies with both SDSS and GAMA spectroscopy, the SDSS stellar masses are higher than the GAMA stellar masses by a median of 0.08 dex and a median absolute deviation of 0.35 dex. We therefore reduce the masses derived from SDSS observations by 0.08 dex; it is however important to note that due to the width of our mass bins, including or excluding this shift does not impact this work.

2.3. Volume Corrections

Our sample is drawn from the SDSS and GAMA spectroscopic surveys, both of which comprise several subsets with different magnitude limits. The sample is composed of observations from the SDSS Legacy Survey ($r_{\text{petro}} < 17.77$, Strauss et al. 2002), the low redshift component of SDSS BOSS ($r_{\text{petro}} < 19.6$, Dawson et al. 2013), and the GAMA second public release

($r_{\text{petro}} < 19.4$ or $r_{\text{petro}} < 19.0$, depending on the region; see [Liske et al. 2015](#)). To convert this sample from magnitude-limited to volume-limited, we adopt the classical $1/V_{\text{max}}$ correction to simulate a volume-limited sample.

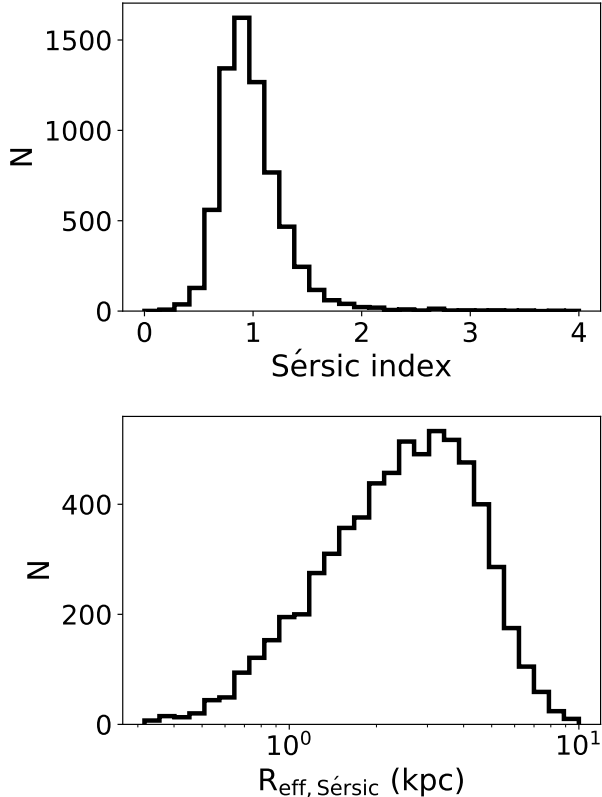


Figure 2. *Top:* The distribution of Sérsic indices over the dwarf sample. The majority of the dwarfs are well-described by an exponential ($n = 1$) profile. *Bottom:* The distribution of effective radii in the sample, as measured from the Sérsic fits.

As all of the galaxies in our sample are low mass, none have maximum observable redshifts for which the observed-frame r -band lies outside of the wavelength range of the (SDSS or GAMA) optical spectrograph. We are thus able to compute the maximum redshift at which the observed r_{SDSS} Petrosian magnitude lies within the spectroscopic selection, z_{max} , directly from the spectra using the public filter response curves measured for SDSS in 2001¹. We use the catalog SDSS and GAMA r_{SDSS} Petrosian magnitudes to compute z_{max} . Though the spectroscopic observations span a considerable range in time, it has been shown that the SDSS

r -band filter transmission curve has evolved by less than 0.01 mag ([Doi et al. 2010](#)). We therefore use the fiducial SDSS transmission curve for all galaxies.

We remove galaxies for which $z \geq z_{\text{max}} + 0.005$ or $z_{\text{max}} < 0.005$ (recall that our minimum redshift cut is $z = 0.005$), as these conditions suggest that there is a problem with the catalog photometry or spectroscopy. From inspection, these are largely comprised of cases where a large galaxy has been erroneously divided into several “low-mass galaxies” during image segmentation (i.e. shredding, see [Blanton et al. 2011](#)).

To validate our directly computed z_{max} values, we compare the distribution of stellar masses in our sample, as weighted by $1/V_{\text{max}}$, to published stellar mass functions in the literature. We report the stellar mass function normalized over our sample mass range; that is, $\tilde{\phi}(\log_{10}(M_*/M_\odot)) \equiv C_0 dN/d(\log_{10}(M_*/M_\odot))$ where C_0 is a constant defined such that $\int_{7.0}^{9.6} \tilde{\phi}(x) dx = 1$.

The top panel of [Figure 1](#) shows this normalized stellar mass function of each magnitude-limited subset in our sample as dashed-line curves. The distribution over the full sample is shown by the thick blue lines, while the original unweighted stellar mass distribution of the sample is shown by the filled grey histogram. The double Schechter fit of [Wright et al. \(2017, from GAMA\)](#) is shown by the solid black line, and the Schechter fit of [Panter et al. \(2007, from SDSS\)](#) by the dashed black line. In both cases, the parametric fits are normalized over the stellar mass range of our sample.

Our $1/V_{\text{max}}$ -corrected stellar mass distribution is in good agreement with the results of [Wright et al. \(2017\)](#), and is somewhat steeper than the mass function of [Panter et al. \(2007\)](#). This is expected, as [Wright et al. \(2017\)](#) includes significantly more galaxies at the stellar mass range of the present sample; the agreement between our normalized stellar mass function and that of [Wright et al. \(2017\)](#) indicates that the $1/V_{\text{max}}$ weights we implement are well-behaved.

3. 1D SURFACE BRIGHTNESS PROFILE MEASUREMENT

With a volume-corrected sample in hand, we now turn to the main objective of this work. The measurement of a 3D shape distribution requires both careful measurements of the projected 1D surface brightness profiles and a framework with which the 3D shape distribution may be inferred from these projected profiles.

We first address our adopted 1D profile measurement scheme. To establish a reasonable initial guess for the centroid position, mean ellipticity, and position angle of the source, we first fit each galaxy with a single Sérsic profile. We also use the Sérsic profile fit to measure an

¹ <http://www.sdss3.org/instruments/camera.php>

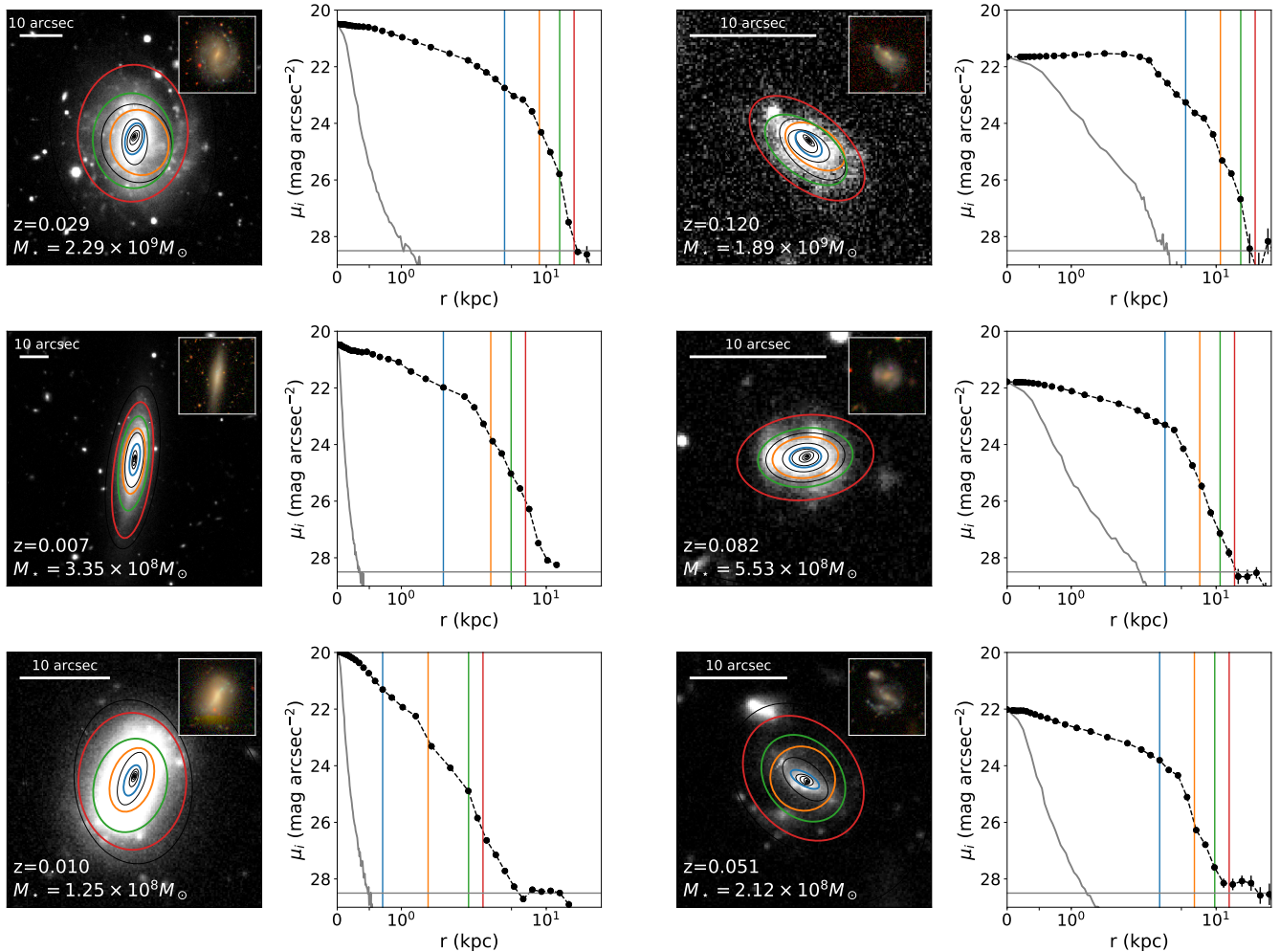


Figure 3. Example 1D surface brightness profiles for galaxies that span the range of stellar mass and redshift in our sample. The lefthand (righthand) columns show galaxies at the low (high) redshift end of the sample, while the rows are ordered in decreasing stellar mass. Each pair of panels shows the i_{HSC} -band image with the measurements at $1R_{\text{eff}}$ (blue), $2R_{\text{eff}}$ (orange), $3R_{\text{eff}}$ (green), and $4R_{\text{eff}}$ (red) overlotted as ellipses. The $gr_{i\text{HSC}}$ -composite RGB image is also shown in the inset panel to more clearly show the morphology of the galaxy. The right panel shows the 1D surface brightness profile of the galaxy; vertical lines show the physical extent at $1-4R_{\text{eff}}$ (same colors as left). We also show the surface brightness of the PSF by the grey curve, and the nominal surface brightness limit of $\mu_i = 28.5 \text{ mag arcsec}^{-2}$ by the grey horizontal line.

effective radius (R_{eff}) for each source. We then extract a 1D ellipticity profile from each galaxy by allowing the isophotal shape to vary with radius.

3.1. Single Sérsic fits

Though a single Sérsic model is not flexible enough to fully describe the structure of dwarf galaxies, it provides a stable and robust model to extract basic flux-weighted structural parameters.

The position angle, ellipticity, centroid from this single Sérsic fit are used to initialize the non-parametric surface brightness profile measurement at R_{eff} . Because dwarf galaxies are often characterized by irregular, off-center star forming regions (Binney & Tremaine 2008), an inflexible and monotonically decreasing model is nec-

essary to establish a reliable galaxy centroid. We additionally adopt the Sérsic-derived effective radius as R_{eff} throughout the paper. In Figure 2, we show the distribution over Sérsic index (top) and effective radius (bottom) for our sample. The dwarfs tend to be well-described by an exponential ($n = 1$) profile, with a median [25th, 75th percentile] Sérsic index of 0.94 [0.79, 1.1]. Their effective radii are typically a few kpc, with a median [25th, 75th percentile] value of 2.5 kpc [1.6, 3.7 kpc], though we note that there is a strong relationship between stellar mass and effective radius.

3.2. Non-parametric Surface Brightness Profiles

Though a single Sérsic fit provides a reasonable initial guess for their surface brightness profiles, dwarf galaxies

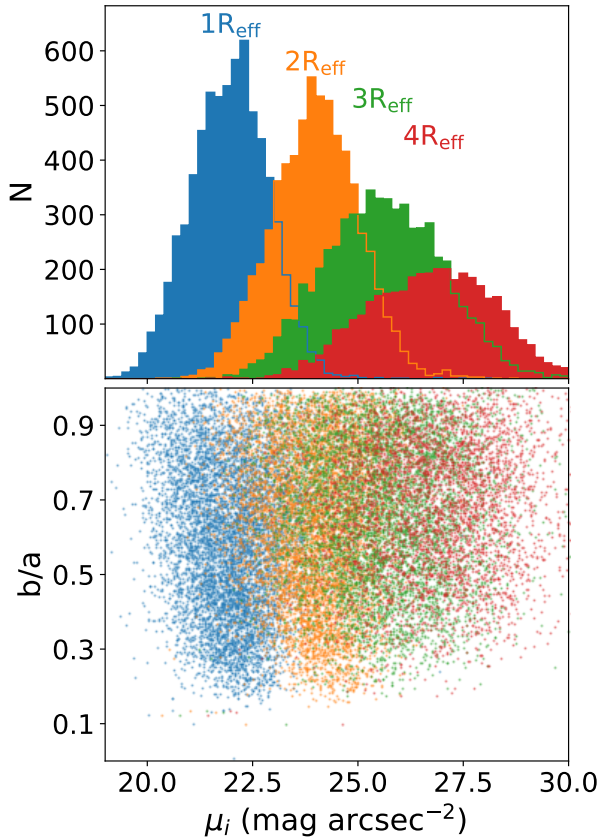


Figure 4. *Top:* the distribution of surface brightness measured at $1-4R_{\text{eff}}$, as labeled. *Bottom:* surface brightness versus projected axis ratio, again colored by measurement radius. Though some measurements are below our nominal surface brightness limit of $\mu_i = 28.5 \text{ mag arcsec}^{-2}$, these comprise only $\sim 7\%$ of ellipticity measurements, and their inclusion does not have a statistically significant effect on the overall ellipticity distribution.

are rich in substructure, and not well-described by a single Sérsic profile. Single Sérsic profiles are also unable to trace changes in ellipticity as a function of radius, by definition.

In order to better describe the complex structure of low mass galaxies, and to test whether ellipticity changes as a function of radius, we adopt a more flexible non-parametric method to measure the 1D surface brightness profiles of the galaxies in our sample. We use the method introduced by Huang et al. (2018a), which is based on the IRAF Ellipse algorithm (Jedrzejewski 1987), and allows ellipticity ϵ , central position $(x_c, y_c)^2$, and position

² We allow the centroid to drift in order to accommodate the presence of off-center starforming regions that may dominate the light near the center of the galaxy. At the radii we consider for this work, the ellipticity distribution does not change significantly when the centroid is held constant or left free.

angle PA to vary as a function of semi-major axis a . The exceptional depth of the HSC-SSP imaging allows us to fit profiles with these parameters free without the fit becoming unstable. To further safeguard against an unstable fit, if the centroid shifts by more than $0.5R_{\text{eff}}$ at $r = R_{\text{shift}}$, we disregard the surface brightness profile at $r > R_{\text{shift}}$.

To generate reliable surface brightness profiles, we must first mask out galaxies that are near the target. To do so, we use the method introduced in Kado-Fong et al. (2020, Appendix B) to detect and mask background sources by detecting sources at spatial frequencies that are high relative to the smooth light of the target outskirts. This approach allows us to remove background galaxies that are at small projected distances from the target galaxy, where they are most likely to contaminate measurements of the galaxy outskirts. We also apply a 3σ clipping to the pixel values along each isophote to reduce the impact from other objects. Huang et al. (2018a) and Ardila et al. (in prep.) have shown that this method works well even for massive galaxies with extended stellar halos. We also adopt a moderately large multiplicative step size of $(a_{n+1} - a_n)/a_n = 0.2$ to help stabilize the ellipticity measurement in the outskirts of the galaxy. In Figure 3, we show example 1D profiles that span the stellar mass and redshift range of our sample. The left panel of each pair shows the isophote at $1-4R_{\text{eff}}$ plotted over the i_{HSC} -band image. The $griz_{\text{HSC}}$ -composite RGB image is also shown by the inset panel. The right panel shows the 1D surface brightness profile for each example. The examples decrease in stellar mass from top to bottom, and increase in redshift from left to right. In addition, we show the overall distribution of surface brightness at $1-4R_{\text{eff}}$ for our 1D profile fits in the top panel of Figure 4, and the surface brightness versus ellipticity in the bottom panel. Though we use effective radii (and multiples thereof) in this work, we have also verified that using fixed physical radii does not change our results.

At $4R_{\text{eff}}$, the farthest extent to which we measure ellipticity profiles, the median surface brightness is $\langle \mu_i \rangle = 26.8 \text{ mag arcsec}^{-2}$, significantly brighter than our surface brightness limit. Seven percent of galaxies have a surface brightness of $> 28.5 \text{ mag arcsec}^{-2}$ at $4R_{\text{eff}}$; we do not remove them from the sample, as their inclusion or exclusion from this analysis does not have a statistically significant impact on the overall ellipticity distribution of the overall sample or subsamples considered in this work. To ensure that we are able to reach this nominal surface brightness limit, we examine the residual sky background near our dwarf sample in Appendix A, and find that the sky is slightly uniformly undersubtracted

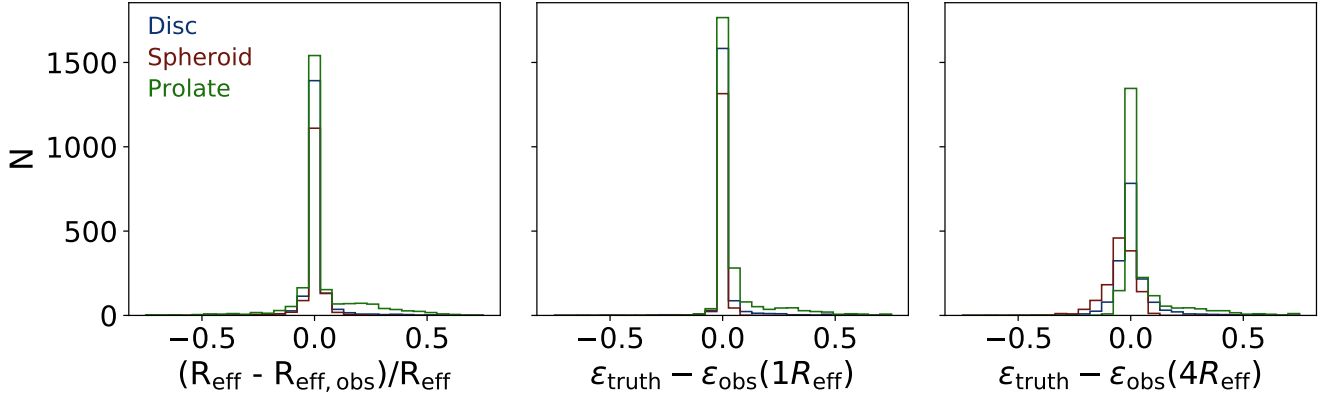


Figure 5. The distribution of errors in recovered effective radius (left), ellipticity at $1R_{\text{eff}}$ (middle), and ellipticity at $3R_{\text{eff}}$ (right) for an injected population of disk ($[A, B, C] = [1., 0.9, 0.1]$, blue), spheroid ($[A, B, C] = [1., 0.9, 0.9]$, red), and prolate ($[A, B, C] = [1., 0.1, 0.1]$, green) galaxies. Each mock galaxy is assigned a viewing angle drawn isotropically over the sphere, injected into the HSC data with an $n = 1$ Sérsic profile, and recovered with our pipeline. In each panel, the text shows the 5th, 25th, 50th, 75th, and 95th percentile of the distribution.

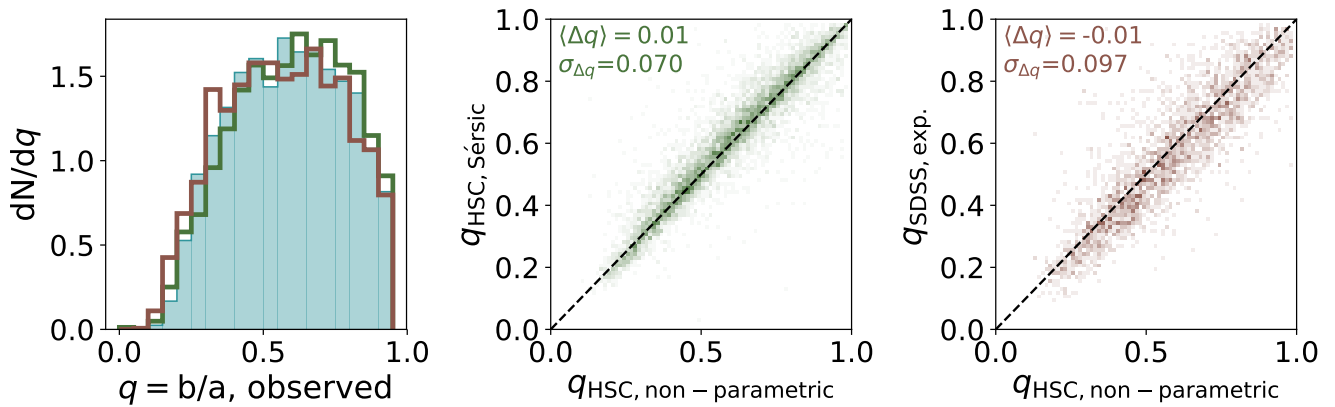


Figure 6. *Left:* the observed distribution of projected axis ratio, $q = b/a$, for the HSC non-parametric measurements (filled teal histogram), HSC Sérsic measurements (green histogram), and SDSS catalog measurements (derived from exponential fits, brown histogram). All three measurements are in good agreement; we find that the mean difference in measured q ($\langle \Delta q \rangle$) and the standard deviation of this difference ($\sigma_{\Delta q}$) are $(\langle \Delta q \rangle, \sigma_{\Delta q}) = (0.017, 0.71)$ and $(\langle \Delta q \rangle, \sigma_{\Delta q}) = (-0.01, 0.10)$ for the HSC Sérsic measurements and SDSS catalog exponential measurements, respectively. In the middle panel we plot the non-parametric measurements at $1R_{\text{eff}}$ against the HSC Sérsic measurements, while in the right panel we show the same non-parametric measurements at $1R_{\text{eff}}$ against the SDSS exponential measurements, for galaxies in the SDSS catalog.

near our dwarfs, corresponding to a surface brightness difference of $\Delta\mu_i \lesssim 0.02 \text{ mag arcsec}^{-2}$ at $\mu_i = 28.5 \text{ mag arcsec}^{-2}$. We thus confirm that the profiles are well-recovered down to our nominal surface brightness limit, and that the residual sky does not affect the shape measurements made in the outskirts of the galaxies.

3.2.1. The Impact of the Point Spread Function

In many situations, it is important to correct for the effects of the point spread function (PSF) in order to probe the outskirts of galaxies (see, e.g. Trujillo & Fliri 2016). In this work, we expect that the effect of the PSF

does not significantly affect our results for the following reasons.

First, due to the high resolution of the HSC imaging, the region of interest for our sample ($r > R_{\text{eff}}$) is not strongly affected by the smearing effect of the finite seeing (the median seeing is $i_{\text{HSC}} \sim 0.6$, Aihara et al. 2019), even at the high redshift end of our sample. To visually demonstrate the size of the PSF with respect to the scale of the profile measurements, in Figure 3 we plot the profile of the PSF in grey. Second, it is important to note that because the cores of dwarfs are intrinsically fainter

than those of their more massive analogs, the effect of scattered light is smaller for a fixed surface brightness limit. The theoretical HSC PSF model of [Coupon et al. \(2018\)](#), which was derived via optical tracing of the instrumental and atmospheric PSF, also shows that the large angular-scale wing of the HSC PSF should not affect measurements made in the outskirts for a sample such as the one considered in this work.

To affirm the above statements quantitatively, we apply a series of tests to the sample. First, we find that the ellipticity distribution (at all radii) does not change significantly as a function of redshift; one expects that the effect of the PSF would become more pronounced for higher redshift targets. Second, we re-fit our galaxies with the single Sérsic model described in [Section 3.3.1](#) convolved with the PSF produced from the HSC-SSP data reduction pipeline. This is a standard technique used to account for the effect of the PSF when using a parametric model (for a review, see [Knapen & Trujillo 2017](#)). We find that the ellipticity as measured with this convolved Sérsic model and the non-parametric ellipticity measurements at $1R_{\text{eff}}$ are offset by $\mu_{\Delta\epsilon} = -0.030 \pm 0.001$, where $\Delta\epsilon = \epsilon_{1R_{\text{eff}}} - \epsilon_{\text{conv}}$. This shift is statistically significant, but not large enough to impact our results.

This is not to say that the effect of the PSF is generically unimportant for low surface brightness science in HSC images – at $r \gtrsim 30$ kpc and $z \sim 0.1$, [Wang et al. \(2019\)](#) found that the extended HSC PSF can account for up to 40% of the flux in the stacked profile of galaxies at $10^{9.2} < M_{\star}/M_{\odot} < 10^{9.9}$ in HSC-SSP. At $r \lesssim 20$ kpc with the bulk of the sample sitting at $z < 0.1$, however, the PSF has a much less significant effect. In particular, [Figure 9](#) in [Wang et al. \(2019\)](#) shows that the impact of the PSF, which depends both on the central surface brightness and concentration of the galaxy, should be small for our sample, which is populated by dwarf galaxies with low central surface brightnesses (relative to massive galaxies) and exponential profiles. For a dwarf with an exponential profile and a central surface brightness of $\mu_i \sim 20$ mag arcsec $^{-2}$, the extended wings of the HSC PSF appear at around a scale of 2 arcsec and a surface brightness of 27 mag arcsec $^{-2}$. At scales comparable to $4R_{\text{eff}}$, this effect will be even smaller. We thus do not expect that the PSF will affect the results presented in this work.

3.3. Profile Measurement Validation

In order to test the validity of our inferred size and ellipticity profiles, we perform several mock galaxy injection tests. In particular, we first confirm that we can recover the ellipticity of Sérsic profiles injected at

low surface brightness without significant bias. Then, we compare our non-parametric measurements of ellipticity at $1R_{\text{eff}}$ to both the parametric measurements of our Sérsic fits to the HSC data and published ellipticity measurements from SDSS imaging to verify that there is no systematic shift between the parametric and non-parametric measurements.

3.3.1. Recovery of Injected Sérsics

First, we inject mock galaxies composed of a single Sérsic profile, the parameters of which (effective surface brightness, effective radius, and intrinsic axis ratios) are drawn from a known distribution, into the HSC co-adds. The surface brightness of the mock galaxies is set to cover the same range as the real galaxies, and the Sérsic index is fixed at $n = 1$ (exponential) for all galaxies. The position of the mock galaxies are selected to be empty locations where there are no detections in any of the five HSC bands, but no other constraints are made on the galaxy placement. These mock galaxies should therefore be affected by imaging artifacts, background galaxies, and residual astrophysical fore/background (e.g. galactic cirrus) in the same way as are the real galaxies in our sample.

[Figure 5](#) shows the injected and recovered distributions of the galaxy structural parameters. We find that the properties of the injected galaxies in this simple test are well-recovered: at $4R_{\text{eff}}$, for 75% of cases the ellipticity of the mock galaxy is recovered to better than $|\epsilon_{\text{truth}} - \epsilon_{\text{obs}}| \leq 0.065$. Crucially, decreasing surface brightness does not significantly bias our ellipticity measurement. In [Figure 4](#), we show the surface brightness distribution of the real galaxy 1D profiles measured at 1-4 R_{eff} . The lower envelope of the projected axis ratio distribution clearly increases with increasing radius (and therefore decreasing surface brightness). We do not find such a trend for the injected disk population, which samples b/a uniformly, over the same range in surface brightness.

While we do not test for the impact of asymmetric features that are not captured by a single Sérsic model, this test verifies that the ellipticity profile is well-recovered in HSC imaging conditions across a range of different injected distributions.

3.3.2. Comparison to parametric b/a measurements

In order to capture the often irregular and asymmetric structure of dwarf galaxies, our non-parametric profile fits allow many parameters to vary as a function of semi-major axis. Thus, it is important to compare our non-parametric measurements of ellipticity to measurements of the same quantity using a more rigid model.

In the left panel of Figure 6, we show the distribution over the observed axis ratio, $q = b/a = 1 - \epsilon$, as measured from the non-parametric ellipticity profiles at R_{eff} (filled teal histogram), from Sérsic fits to the HSC-SSP imaging (green, unfilled), and from exponential fits to SDSS imaging of the same galaxies. We find that our non-parametric measurements are in good agreement with both the Sérsic profile fits ($\sigma_{\Delta q} = 0.07$) and the SDSS exponential profile fits ($\sigma_{\Delta q} = 0.101$). The increase in scatter with respect to the SDSS measurements is not unexpected, as the SDSS imaging is significantly shallower and fit with a less flexible model (i.e. where the Sérsic index is fixed to $n = 1$). The lack of bias as a function of projected axis ratio, however, is a good indication that our non-parametric measurements obtain reasonable results despite their flexibility.

4. 3D SHAPE INFERENCE

Let us assume that the 3D shapes of each galaxy in our sample (or subsample) are drawn from a single distribution over the intrinsic axis ratios B/A and C/A , given by $P(\vec{\alpha})$ where $\vec{\alpha}$ is some set of parameters that describes the distribution of B/A and C/A . The projected axis ratio, q , for any given ellipsoid is determined solely by the observer's viewing angle, (θ, ϕ) . That is to say, the projected axis ratio q can be written as $q = \mathcal{F}(B/A, C/A, \theta, \phi)$.

The analytic expression for \mathcal{F} was presented by Simonneau et al. (1998), and is reproduced below. First, $(ab)^2$ and $(a^2 + b^2)$ can be rewritten as follows:

$$a^2b^2 = f^2 = (C \sin \theta \cos \phi)^2 + (BC \sin \theta \sin \phi)^2 + (B \cos \theta)^2, \quad (1)$$

$$a^2 + b^2 = g = \cos^2 \phi + \cos^2 \theta \sin^2 \phi + B^2(\sin^2 \phi + \cos^2 \theta \cos^2 \phi) + (C \sin \theta)^2 \quad (2)$$

We now define the quantity h to be

$$h \equiv \sqrt{\frac{g - 2f}{g + 2f}}, \quad (3)$$

such that it may be shown that

$$\frac{b}{a} = \frac{1 - h}{1 + h} \quad (4)$$

Because the distribution of viewing angles is known to be isotropic on the surface of the sphere, we can predict the projected distribution of q given a choice of intrinsic shape distribution characterized by $\vec{\alpha}$ by sampling ϕ and θ as follows:

$$\begin{aligned} \phi &\sim \mathcal{U}[0, 2\pi] \\ \nu &\sim \mathcal{U}[0, 1] \\ \theta &= \cos^{-1}(2\nu - 1) \end{aligned} \quad (5)$$

For simplicity, we first consider a normal distribution over both B and C , such that the 3D shape distribution can be described by the parameters $\vec{\alpha} = \{\mu_B, \mu_C, \sigma_B, \sigma_C\}$. We find that the data are well-described by this relatively simple model, and that the fit is not significantly changed or improved by a more complex model (as motivated by Zhang et al. 2019, see Appendix B).

Armed with this framework, we are able to quickly estimate the distribution of projected axis ratios for a given choice of $\vec{\alpha}$. This can then be compared cheaply to the observed distribution of q by adopting a Poisson likelihood,

$$\ln p(q|\mu_B, \mu_C, \sigma_B, \sigma_C) = \sum_i n_i \ln m_i - m_i - \ln n_i!, \quad (6)$$

where n_i is the observed count where $0.04i < q \leq 0.04(i + 1)$ and m_i is the predicted count in the same range. Though this likelihood is in principle sensitive to the adopted bin size, for our sample we find that the results are not significantly affected by reasonable choices for the bin width. For each step, we choose the binsize from a uniform distribution bounded by $[0.03, 0.1]$. The minimum width is chosen such that for the minimum sample size that we consider ($N = 700$, see Section 5.1), for a uniform distribution of projected axis ratio the standard deviation of the counts in a given bin is expected to be $\sim 20\%$ of the mean bin count.

We adopt a flat prior for all model parameters. The prior over μ_B and μ_C is set purely by the physical boundaries:

$$p(\mu_B) = \begin{cases} 1 & \text{if } 0 < \mu_B < 1 \\ 0 & \text{otherwise} \end{cases} \quad (7)$$

we additionally constrain $\mu_C \leq \mu_B$ to maintain the order of axes,

$$p(\mu_C) = \begin{cases} 1 & \text{if } (0 < \mu_C < 1) \quad (\mu_C \leq \mu_B) \\ 0 & \text{otherwise,} \end{cases} \quad (8)$$

additionally, when sampling from a given α , we disregard cases where $C > B$.

We implement the same flat prior over σ_B and σ_C :

$$p(\sigma_X) = \begin{cases} 1 & \text{if } 0 < \sigma_X < 0.5 \\ 0 & \text{otherwise} \end{cases} \quad (9)$$

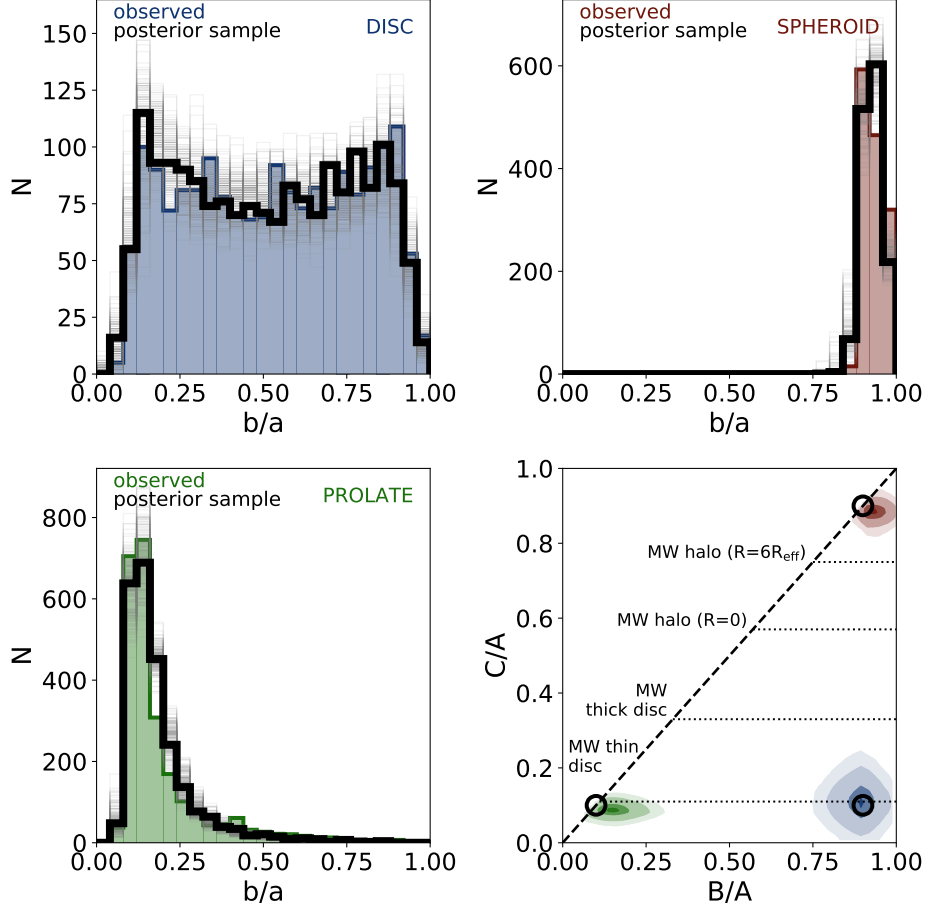


Figure 7. For the injected ellipsoid populations described in Figure 5, we infer the 3D shape distribution of the population from the recovered projected axis ratios. In each column, we show the inference results for our injected populations of disk ($[A, B, C] = [1., 0.9, 0.1]$, left), spheroid ($[A, B, C] = [1., 0.9, 0.9]$, middle), and prolate ($[A, B, C] = [1., 0.1, 0.1]$, right) galaxies. The top row shows the recovered b/a distribution as filled histograms and the posterior b/a sample as unfilled black histograms. The bottom row shows the distribution of the posterior sample over the intrinsic axes (B and C). The black circle shows the true position of the intrinsic axes. For physical context, we show the C/A values measured for the Milky Way disk-halo system as measured by Schönrich & Binney (2009) and Iorio & Belokurov (2019). The dashed black line shows the definitional boundary of $B = A$.

where $X \in (B, C)$. Here, the upper limit is set so that the distribution is contained largely within the physically admissible region.³

We can then write the posterior probability distribution as $p(\vec{\alpha}|q_{\text{obs}}) \propto p(q_{\text{obs}}|\vec{\alpha})p(\mu_B)p(\mu_C)p(\sigma_B)p(\sigma_C)$. To sample efficiently from this distribution, we use the Markov Chain Monte Carlo ensemble sampler implemented in emcee (Foreman-Mackey et al. 2013). For each case discussed in the work, we run the sampler with 32 walkers and 3000 moves. We verify that the walkers have converged and discard the first 150 moves of each.

³ We furthermore find that none of our data suggest σ_X near 0.5, indicating that this choice of boundary does not affect our results.

4.1. Validation: Comparison to Sérsic Populations

In order to test our 3D inference framework, we return to the injected Sérsic populations of Section 3.3.1. These tests have the advantage of incorporating both major sources of uncertainty in the final 3D shape inference: the uncertainty in the 1D profile measurement (due to, e.g., neighboring galaxies, residual sky background) and in the 3D shape inversion problem.

In Figure 7, we show the recovered distribution of projected axis ratios by the colored histograms: blue for the disk population, red for spheroidal, and green for prolate. The distribution of projected axis ratios generated by sampling the posterior is shown by the thick black stepped curve in each (the thin black lines show individual draws from the posterior). The lower right panel

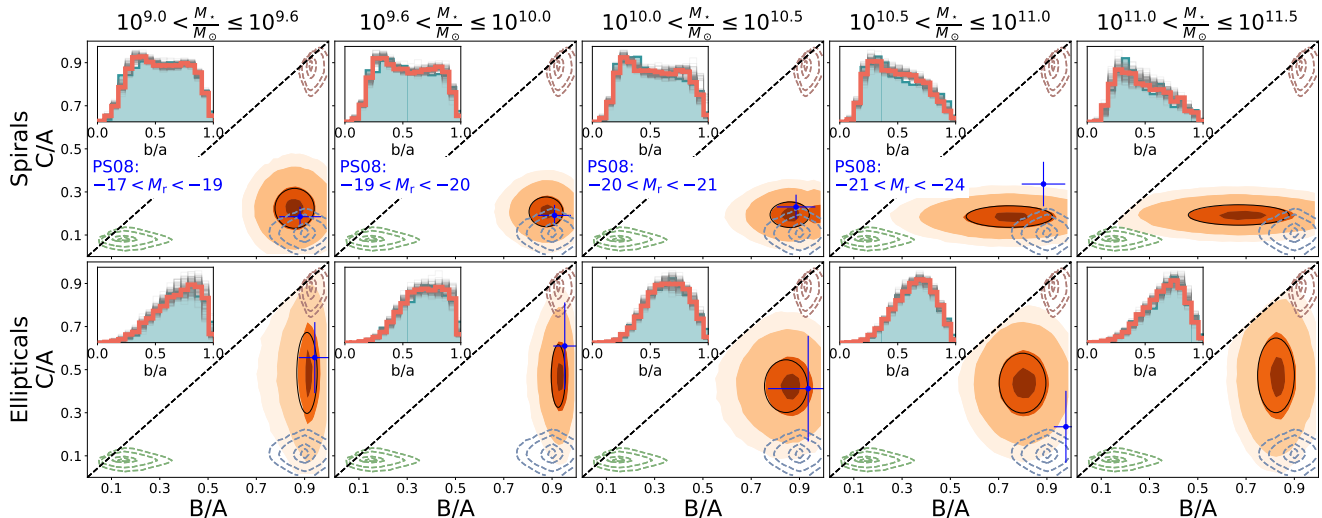


Figure 8. Inferred 3D shape distributions as a function of stellar mass (increasing towards top) and morphology (spirals at top, ellipticals at bottom), using SDSS catalog measurements following the morphology criterion of Padilla & Strauss (2008). In each panel, the filled contours show the inferred 3D shape distribution using our method, while the blue errorbars show the mean and standard deviation of the 3D shape distribution from Padilla & Strauss (2008) in roughly analogous bins of r_{SDSS} -band absolute magnitude. Our inferred shape distributions are in general agreement with those of Padilla & Strauss (2008), taking into account that the absolute magnitude cuts are not equivalent to our cuts in stellar mass. In particular, the highest luminosity bin of Padilla & Strauss (2008), where our inference is in significant disagreement, extends to $M_* \sim 10^{12} M_{\odot}$. We also show the same contours for the pure disk, prolate, and spheroid Sérsic population presented in Figure 7 by the dashed blue, green, and red curves.

of Figure 7 shows the distribution of this posterior sample in the intrinsic B-C axis space; the colored contours show the regions that contain 0.34^2 , 0.68^2 , 0.95^2 , and 0.99^2 of the distribution (corresponding to the 0.5σ , 1σ , 2σ , and 3σ regions for a multivariate normal distribution). The black circles show the true value of μ_B and μ_C .

When the true value of μ_B and μ_C are sufficiently distant from the boundary, we find that we are able to recover their values very well, as seen for the disk population in blue. However, we find that our inferred values are biased when the true value is close to the imposed boundary ($B/A=C/A$) of the problem, as is the case for the spheroidal and prolate populations. Based on the shape distributions inferred by studies at higher masses (see, e.g. Padilla & Strauss 2008; van der Wel et al. 2014) and by studies of ultra diffuse galaxies in clusters (Burkert 2017; Rong et al. 2019), as well as the shape distributions measured from cosmological simulations (Pillepich et al. 2019), it is unlikely that real galaxies are characterized by extreme distributions at the $B=C$ boundary.

All of our injected Sérsic galaxies are drawn from a 3D shape distribution where $\sigma_B = 0$ and $\sigma_C = 0$; the inferred σ_B and σ_C in these test cases should then pro-

vide a lower limit on the intrinsic dispersion to which we are sensitive.⁴

4.2. Validation: Comparison to Padilla & Strauss (2008)

Before applying this shape inference framework to our sample of HSC dwarfs, we want to confirm that our method can reproduce published 3D shape distributions of higher mass galaxies. Towards this end, we use SDSS catalog shape measurements to infer 3D shape distributions from data that are analogous to those of Padilla & Strauss (2008), who use SDSS catalog measurements to estimate the 3D shape distribution of galaxies with stellar masses of $M_* \gtrsim 10^9 M_{\odot}$.

For a linear combination of an exponential profile (i.e., a Sérsic profile with index $n = 1$) and a deVaucouleurs profiles (i.e., a Sérsic profile with index $n = 4$), the SDSS photometric catalog provides the weight assigned to the $n = 4$ component as f_{deV} (Abazajian et al. 2004). Padilla & Strauss (2008) separate their sample into a subset of spiral galaxies, wherein $f_{\text{deV}} < 0.8$, and elliptical galaxies, wherein $f_{\text{deV}} > 0.8$, and evaluate their 3D shape distributions independently. Using the SDSS

⁴ Because the Sérsic profiles are quite different from real galaxies, we do not attempt to deconvolve the error in σ_B and σ_C for the real sample using these test cases in this work.

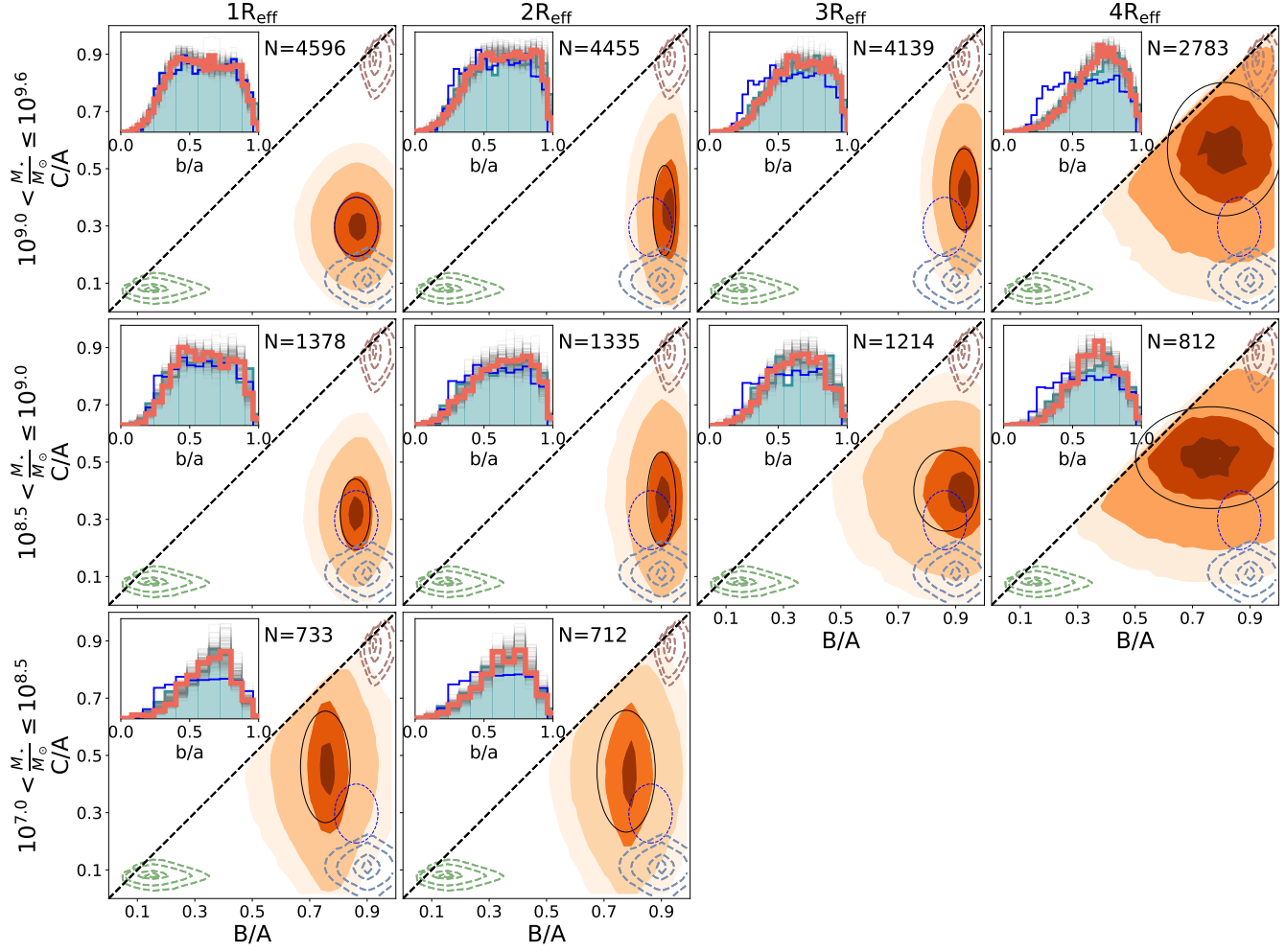


Figure 9. For bins in increasing stellar mass (rows) and measurement radius (columns), the distribution of inferred axis ratios B/A and C/A for the dwarf sample. Each panel shows the distribution of intrinsic axis ratios in orange. The black ellipses show the 1σ region of the maximum a posteriori estimate, $\max_{P(\vec{\alpha}|b/a)} \vec{\alpha}$. We also show the same contours for the pure disk, prolate, and spheroid Sérsic population presented in Figure 7 by the dashed blue, green, and red curves. The black line shows the $B/A=C/A$ definitional boundary. Each inset panel shows the observed axis ratio, $b/a = 1 - \epsilon$, distribution as the solid teal histogram. The distribution of b/a produced by the posterior sample in B/A and C/A is shown by the orange unfilled histogram; individual samples from the posterior are shown by the grey unfilled histograms.

DR16 catalog, we divide the sample of galaxies with $z < 0.05$ and $M_* \gtrsim 10^9 M_\odot$ in the same manner (Ahumada et al. 2019).

We then use the 3D shape inference method described above to estimate the distribution over intrinsic axes B and C for bins of approximately 0.5 dex in stellar mass (the first mass cut is set at $\log_{10}(M_*/M_\odot) = 9.6$ so that the lowest mass bin considered is equivalent to the highest mass bin of our sample).

The results of this inference, with the roughly equivalent r_{SDSS} -band absolute magnitude bins of Padilla & Strauss (2008) overlaid, are shown in Figure 8. Each panel inset shows both the observed distribution of b/a , measured via the non-parametric profile construction

described in Section 3, by filled teal histograms. We then overplot the distribution of projected b/a generated from sampling the MCMC chain in grey, i.e. $\vec{\alpha}_i \sim P(\mu_B, \mu_C, \sigma_B, \sigma_C | b/a)$. The distribution of b/a over all of these samples is then shown by the thick orange curve. In the main panel, we show the analogous distribution in the intrinsic axes (B - C) plane. Here, the same samples from the posterior are shown by the orange filled contour. The dashed colored curves are the contours of the pure disk, spheroid, and prolate Sérsic populations shown in the lower right panel of Figure 7.

Due to the differences in data used and the imperfect mapping between stellar mass and absolute magnitude, we do not expect that the inferences will be statistically

identical. However, we find good agreement between our results and those of Padilla & Strauss (2008) for all but their brightest bin at $-21 < M_r < -24$, which includes a significantly wider mass range than our most similar bin. Having reproduced the 3D shape distribution of this literature sample, and of the mock galaxies injected into HSC imaging, we proceed to apply the shape inference technique to the dwarf sample at hand.

5. RESULTS

The HSC-SSP imaging has both the surface brightness sensitivity to reliably measure the ellipticity profile of individual galaxies out to $3R_{\text{eff}}$ and the on-sky area necessary to build a sample large enough to infer the 3D shape distribution.

Before proceeding, we note that the transition from thin disk to thick disk to spheroid does not have a well-defined boundary. To put our results into context, we provide the intrinsic axis ratios of the Milky Way disk and halo system. Assuming an exponentially declining disk, the Milky Way has a disk scale length of 2.5 kpc, a thin disk scale height of 270 pc, and a thick disk scale height of 820 pc. This corresponds to an axis ratio of $C/A = 0.11$ for the MW thin disk, and $C/A = 0.33$ for the MW thick disk (Schönrich & Binney 2009). The MW stellar halo becomes increasingly spheroidal as a function of radius in the range of $0.57 \leq C/A \leq 0.75$ (Iorio & Belokurov 2019).

5.1. 3D Shape as a function of Stellar Mass and Radius

We first consider the change in the galaxy 3D shape as a function of stellar mass and radius. Previous studies have found that the high mass end of our sample ($10^9 < M_*/M_\odot < 10^{9.6}$) are composed largely of (thick) discs (Padilla & Strauss 2008; Sánchez-Janssen et al. 2010; van der Wel et al. 2014); 3D shapes beyond $1R_{\text{eff}}$ or at lower masses have not been measured for general dwarf samples.

First, we consider the distribution of observed b/a as measured at $1R_{\text{eff}}$, $2R_{\text{eff}}$, $3R_{\text{eff}}$, and $4R_{\text{eff}}$ for bins of stellar mass in Figure 9. Each panel shows the number of measurements made for each slice in radius and stellar mass. From tests with Sérsic populations, we find that the recovered values of σ_B and σ_C increase significantly at $N \lesssim 700$; we therefore do not consider subsets where $N < 700$ (see Appendix C).

From the observed distribution alone, we see first that the distribution of projected axis ratios becomes increasingly more concentrated at large values of b/a as we consider larger radii. This is consistent with a shift towards more spheroidal shapes; indeed, in Figure 9, we see that

the high-mass dwarfs are consistent with a thick disk at $1R_{\text{eff}}$, and shift towards the spheroidal extreme at $3R_{\text{eff}}$ and $4R_{\text{eff}}$. We note that a minority of the galaxies in the sample have bars at $1R_{\text{eff}}$ – though these bars clearly do not dominate the signal (bars are intrinsically prolate, with $\mu_B \sim \mu_C \sim 0.3$ Compère et al. (2014); Méndez-Abreu et al. (2018)), it is likely that they contribute to the recovered triaxiality of the sample. Indeed, though the dwarfs are only slightly triaxial ($\mu_B \sim 0.75$ at all masses and radii), we find that a purely oblate model is a significantly worse fit to the data.

We see relatively little change in the intrinsic shape distribution of galaxies at $10^{8.5} < M_*/M_\odot \leq 10^{9.0}$ and those at $10^{9.0} < M_*/M_\odot \leq 10^{9.6}$. Both show $\mu_C(1R_{\text{eff}}) \sim 0.3$, and shift towards progressively larger μ_C with increasing radius. In our lowest mass bin, we see a hint that the shape distribution shifts dramatically, towards lower μ_B and μ_C (i.e. away from the pure disk region). Though this behavior is not unexpected, as lower mass galaxies are expected to be increasingly dispersion dominated (see, e.g. Wheeler et al. 2017; Pillepich et al. 2019), we caution that we are not complete at this mass bin, and that the number of galaxies in our lowest mass bin is significantly lower ($N \sim 700$), which may lead to an overestimation of σ_B and/or σ_C (see Appendix C).

5.2. 3D Shape and Galaxy Color

At higher masses, we reproduce in Figure 8 the divergence in 3D shape distribution of spiral and elliptical galaxies seen in Padilla & Strauss (2008). One can then reasonably expect to see a similar trend at $\approx 1R_{\text{eff}}$ when our sample is divided between red and blue galaxies. We divide our sample at $(g - i)_{\text{SDSS}} = 0.9$, chosen as the midpoint between the blue sequence and red cloud for this choice of color and stellar mass range⁵.

We show the 3D shape distribution for the highest mass bin in Figure 10 as a function of radius, again at $1R_{\text{eff}}$, $2R_{\text{eff}}$, and $3R_{\text{eff}}$ from left to right. The left column shows the results at $1R_{\text{eff}}$. Indeed, in the leftmost column we see that the red galaxies are at preferentially larger C/A with respect to blue galaxies, similar to Figure 8 when the sample is split between spiral and elliptical galaxies.

At larger radii, however, we find that the blue and red galaxies occupy the same region in the B-C plane. While the red galaxies show little shape change with radius, the distribution of blue galaxies increases in σ_C and

⁵ Because the red sequence is relatively unpopulated at this mass range, we choose the division using the SDSS catalog and a somewhat broader range in stellar mass $M_* \lesssim 10^{10.5} M_\odot$

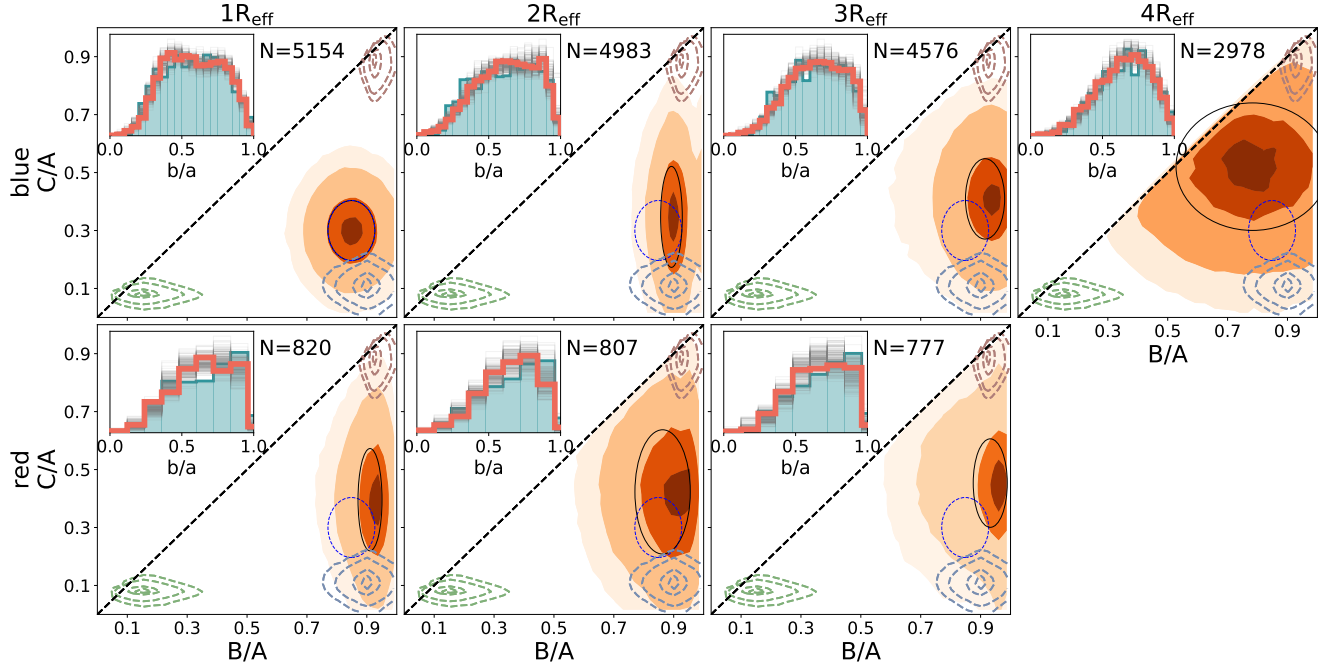


Figure 10. For dwarfs with $M_* > 10^{8.5} M_\odot$, the inferred shape distribution for blue ($g - i < 0.90$) and red ($g - i > 0.90$) galaxies as a function of radius. Similar to the trend we see in the analogous mass bin of Figure 8, the 3D distribution of blue galaxies is diskier than the red galaxies at $R = 1R_{\text{eff}}$. At large radii, both blue and red galaxies move towards spheroidal shapes. As in Figure 9, we show the 50th percentile regions of the pure disk, prolate, and spheroid Sérsic population presented in Figure 7 by the dashed blue, green, and red curves.

shifts towards the spheroidal corner (red dashed curve) of parameter space.

5.3. 3D Shape and Environment

Star formation in dwarfs is thought to be quenched by almost entirely environmental means (Geha et al. 2012); it is of interest, then to ask whether populations of field and satellite dwarfs display the same change in 3D shapes as do blue and red dwarfs. For this exercise, we search massive companions ($M_* > 10^{10} M_\odot$) in the NASA Sloan Atlas (NSA) within $\Delta v < 1000 \text{ km s}^{-1}$ and 1 Mpc projected distance. We choose the projected distance cut $d_{\text{NN}} > 1 \text{ Mpc}$ to coincide with the distance at which the dwarf quenched fraction, $f_{\text{quench}}(d_{\text{NN}})$, approaches its field limit $f_{\text{quench}}(d_{\text{NN}} \rightarrow \infty)$ for the mass range considered in Geha et al. (2012, see Figure 4). We additionally consider only galaxies at $z < 0.10$. Though the NSA contains galaxies up to $z = 0.15$, at $z > 0.1$ the satellite fraction begins to drop, indicating that the massive galaxy sample is not sufficiently complete to characterize the environment of the dwarfs in our sample. In Figure 11, we show the 3D shape distribution for field (top row) and satellite (bottom row) dwarfs at $M_* > 10^9 M_\odot$. Unlike the dwarfs separated by color, the satellite and field dwarf samples show roughly the same 3D shape distribution as a function of radius. It is important to note that the difference in σ_B at large radius

between the field and satellite dwarfs is likely unphysical, as the inferred σ_B for these populations is close to or below the estimated σ_B for our zero-scatter disk and spheroid populations (shown in Figure 11 by the dashed contours).

We find that at $1R_{\text{eff}}$, the satellite galaxies scatter towards marginally more spheroidal shapes than do the field galaxies. This effect is similar to the trend seen in Section 5.2 between red and blue dwarfs, but the separation between field and satellite galaxies is relatively small. Though the projected axis ratio distribution of field galaxies and satellite galaxies is significantly different (Kolmogorov-Smirnov p-value ≈ 0.001), we do not see a significant difference between the b/a distribution of field galaxies and blue satellites (KS p-value ≈ 0.29). This is likely due to fact that, for our sample, nearly all red galaxies are satellites of more massive galaxies (Geha et al. 2012). Blue galaxies, on the other hand, are found both as satellites and in the field. It is likely that making a cut on color produces, in effect, a selection of satellite galaxies that have been more processed by the host central.

6. DISCUSSION

6.1. The Emergence of Round Outskirts Around Low-Mass Galaxies

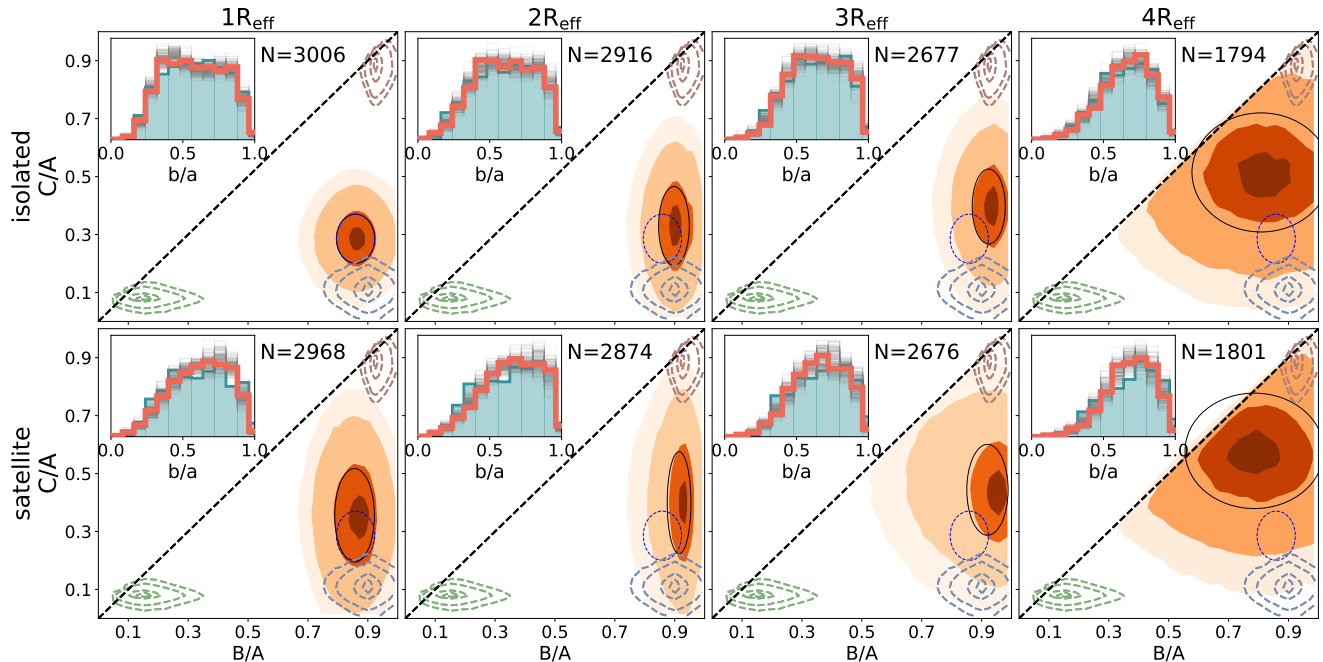


Figure 11. For dwarfs with stellar masses $M_* > 10^{8.5} M_\odot$, the inferred shape distribution for field (distance to nearest neighbor $d_{\text{NN}} > 1\text{Mpc}$) and satellite ($d_{\text{NN}} \leq 1\text{Mpc}$) galaxies. We see negligible difference between satellite and field galaxies; both are consistent with thick discs at $1R_{\text{eff}}$, and C/A increases towards spheroid shapes at larger distances from the galaxy center. As in Figure 9, we show the analogous contours of the pure disk, prolate, and spheroid Sérsic population presented in Figure 7 by the dashed blue, green, and red curves.

At higher masses, stellar halos are generally thought to be the product of a series of minor mergers, which deposit stars at large radii (Amorisco 2017). However, because the stellar-to-halo mass ratio tends to increase as galaxy mass decreases, the dwarfs in our sample are unlikely to accrete a sufficient mass in stars to build a stellar halo via minor mergers alone (Purcell et al. 2007; Moster et al. 2013).

Even though it appears unlikely that dwarfs can accrete a stellar halo via conventional means, it has long been known that dwarfs in the Local Group and M81 Group host a smooth intermediate/old stellar population in their outskirts (see Stinson et al. 2009; Hargis et al. 2020, and references therein). These observations hint at the existence of an in-situ halo formation mechanism at low masses, but this conclusion is obfuscated for two reasons: first the sample is comprised almost entirely of galaxies that are interacting with a more massive companion. Second, such stellar halos have been confirmed for only a few tens of galaxies. In this work, we have presented the first large sample where a clear transition to a round stellar component is detected in the outskirts of dwarfs that are not Local Group members.

In Section 5.1, we presented a set of inferred 3D shapes for a sample of dwarf galaxies as a function of stellar

mass and radius. Due to the depth of the HSC-SSP imaging, we are able to measure ellipticity profiles out to $4R_{\text{eff}}$ for the most massive dwarfs in our sample. Indeed, we see that the structure of the dwarfs are characterized by thick discs at $1R_{\text{eff}}$ and become increasingly spheroidal at large radii, as shown in the top row of Figure 9. For clarity we also show the C/A distribution as a function of radius for the $10^9 M_\odot < M_* < 10^{9.6} M_\odot$ and $10^{8.5} M_\odot < M_* < 10^9 M_\odot$ stellar mass bins in Figure 12. At $1R_{\text{eff}}$, the dwarfs have C/A axis ratios consistent with the Milky Way thick disk, and significantly thicker than the MW thin disk (Schönrich & Binney 2009). This thick disk morphology is in rough agreement with previous measurements for dwarfs in SDSS and the Local Group (Padilla & Strauss 2008; Sánchez-Janssen et al. 2010; Roychowdhury et al. 2013). At $4R_{\text{eff}}$, the dwarfs shapes are of comparable thickness to the inner stellar halo of the MW as measured by Iorio & Belokurov (2019). These results indicate that the dwarf disk-halo interface is similar in structure, if not origin, to more massive galaxies.

Though they are not expected to form through minor mergers, the existence of round stellar outskirts around dwarfs is not unexpected theoretically. Dwarf galaxies sit in shallow potential wells, and are thus more sensitive to the effects of star formation feedback than their

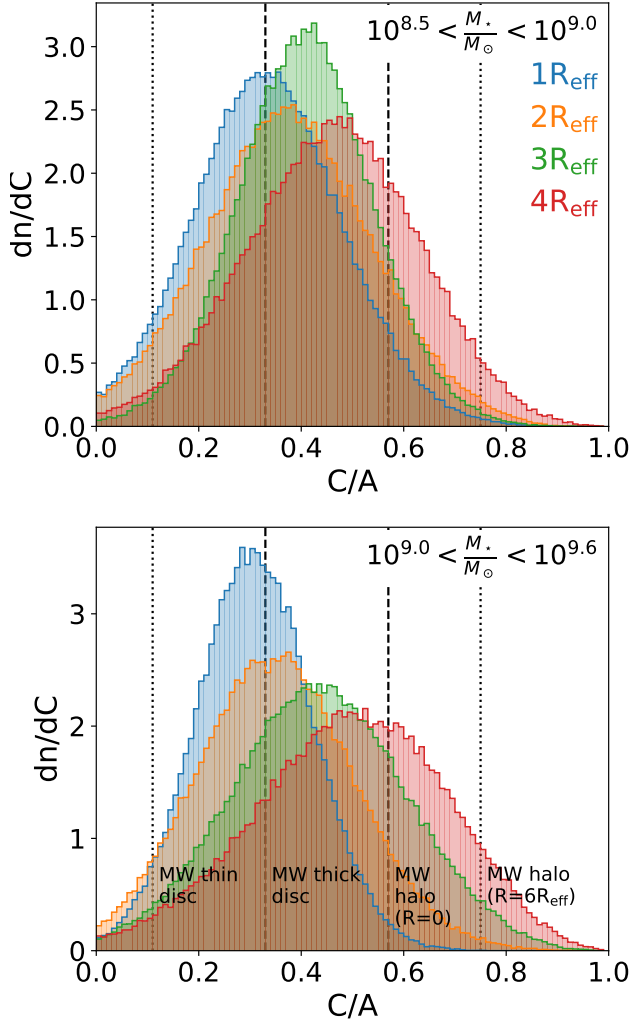


Figure 12. The change in galaxy thickness (C/A) as a function of radius for $10^9 < M_*/M_\odot < 10^{9.6}$ (top) and $10^{8.5} < M_*/M_\odot < 10^9$ (bottom). In both cases, the dwarfs become systematically more spheroidal ($C \sim A$, $B/A \gtrsim 0.8$ for all cases) at large radii. For physical context, we also show the C/A axis ratio of the Milky Way thin disk & thick disk (Schönrich & Binney 2009), and the stellar halo at $R = 0$ & $R = 6R_{\text{eff}}$ (Iorio & Belokurov 2019). The MW axis ratios are shown by vertical black lines, as labeled in the bottom panel.

more massive analogs. Stinson et al. (2009) proposed that dwarf galaxies would generically form stellar halos through stellar radial migration, star formation in outflows, and a contraction of the central star-forming region. Similarly, Maxwell et al. (2012) found that stellar feedback could drive sufficient quantities of dense gas to produce a fluctuation in the overall potential and thus build a stellar spheroid through migration (see also El-Badry et al. 2016). The concordance in 3D shape

at large radii for blue and red dwarfs, as shown in Figure 10, and at all measured radii in field and satellite dwarfs, as shown in Figure 11, also suggests that the creation of round outskirts is not driven by an interaction with a more massive halo.

It has also been suggested that dwarf halos could be formed as a result of major mergers between dwarfs (Bekki 2008). However, the detection of an increasingly spheroidal component in the outskirts of our dwarf sample is at odds with this formation mechanism; the major merger rate of dwarfs is likely not high enough to generate enough stellar halos to produce such a population. Simulations suggest that approximately 30% of dwarfs in our stellar mass range outside of the Virial radius of a MW-like object have undergone a dwarf-dwarf major merger in the past 10 Gyr (Deason et al. 2014). Though dwarf-dwarf major mergers were more common in the early universe, due to fading via passive evolution it is unlikely that we would be able to detect such ancient halos. Though the $z = 0$ surface brightness of any given merger-driven stellar halo is dependent on its assembly history, Bekki (2008) finds that their simulated stellar halo reaches ~ 30 mag arcsec $^{-2}$ at $R \sim 2$ kpc. If the stellar halo population had a uniform age of 1 Gyr at the time of halo creation, and was created at a lookback time of 10 Gyr, the stellar halo will have dimmed by 1-2 mag arcsec $^{-2}$ by $z = 0$ from the evolution of the mass-to-light ratio alone (as computed from the FSPS models of Conroy et al. 2009), well below the surface brightness sensitivity of our imaging. Moreover, the intermediate age stellar component often observed at large radii in resolved star studies requires a relatively recent deposition of stars in the outskirts (see, e.g. Zaritsky et al. 2000; Stinson et al. 2009, and citations therein). We thus find it unlikely that major mergers are the sole formation mechanism of low-mass stellar halo formation, though we note that some individual cases are consistent with both star formation feedback and accretion driving stellar halo formation (Pucha et al. 2019). The apparent ubiquity of round stellar outskirts in this work is instead consistent with the proposal that stellar outskirts are formed primarily through in-situ processes.

6.2. Morphological Transformation and Quenching

It has long been observed that the cessation of star formation in dwarfs, their morphological transformation from a disk-dominated to a dispersion-dominated structure, and their proximity to more massive galaxies are all strongly correlated (see, for example, Dressler 1980; Lin & Faber 1983; Postman & Geller 1984; Weinmann et al. 2006; Geha et al. 2012; Kormendy & Bender 2012; Ann 2017).

As shown in the leftmost column of Figure 10, we find that the blue dwarfs in our sample tend towards lower values of C/A than red dwarfs – that is, the blue dwarfs are more consistent with a thick disk, while red dwarfs scatter towards more spheroidal shapes. This is in concordance with the familiar morphology-color dichotomy, and follows the same trend seen in intrinsic shape studies at higher masses (see, e.g. Padilla & Strauss 2008; Rodríguez et al. 2016, and Figure 8). We see a similar trend when separating dwarfs by the projected nearest neighbor distance (within 1000 km s^{-1}), though the shift between satellite and field galaxies is relatively marginal (see leftmost column of Figure 11).

We do not detect a significant difference in the intrinsic shapes of blue satellites and dwarfs in the field. This is in contrast with the shift towards rounder shapes seen in the red galaxy subset (Figure 10) and satellite galaxies (without a color cut, Figure 11). This suggests that morphological transformation operates on a longer timescale than star formation quenching, or that quenching is a prerequisite to the morphological transformation. However, it is important to note our choice of model (a singly-peaked multivariate Gaussian) will necessarily only recover the dominant shape population.

6.3. Comparison with Simulations

Due again to their increased sensitivity to star formation feedback, the 3D shapes of dwarfs are a strong constraint on the feedback prescription of cosmological simulations.

Pillepich et al. (2019) give the distribution of dwarf 3D shapes as measured at twice the stellar half-mass radius. First, we note that our results are in broad agreement with those of Pillepich et al. (2019) in that our 3D shapes are in the disk/spheroidal regime, with essentially no galaxies in the prolate regime (defined by van der Wel et al. (2014) as $B/A < 1 - C/A$). At R_{eff} , the change in our 3D shape distribution is also qualitatively similar to that of Pillepich et al. (2019); as stellar mass decreases, σ_C increases and the distribution shifts towards more spheroidal shapes (as shown in the leftmost column of Figure 9).

However, under the assumption of centrally concentrated star formation, we would expect the half-mass radius to be larger than the half-light radius, implying that a comparison at the same physical radius should occur at $> 2R_{\text{eff}}$. Moreover, the conversion between the i_{HSC} -band surface brightness and the stellar mass distribution is a function of the galaxy’s stellar populations.

Clearly, to make a quantitative comparison, it will require significant effort to put the simulations and observations on equal footing. Nevertheless, the broad

agreement in the shape distribution of dwarfs and its evolution with stellar mass is a promising step.

7. CONCLUSIONS

In this work we have measured the surface brightness and ellipticity profiles of a sample of spectroscopically confirmed dwarfs using imaging from the Hyper Suprime-Cam Subaru Strategic Program (Section 3). We then extended the framework commonly used to infer 3D galaxy shapes (see, e.g., Padilla & Strauss 2008; Roychowdhury et al. 2013; van der Wel et al. 2014; Zhang et al. 2019; Putko et al. 2019) to measure the change in dwarf galaxy shape as a function of radius.

We show that the population of dwarfs in our sample tend to host thick, disk-like structures at $1R_{\text{eff}}$, and evolve towards more spheroidal shapes in their outskirts (see Figure 9). This finding is in agreement with the predicted quasi-spherical shapes of in-situ stellar halos (Stinson et al. 2009).

At $M_* > 10^{8.5} M_{\odot}$, blue dwarfs tend to be diskier than red dwarfs near their centers (i.e. at $R=1R_{\text{eff}}$, left panel of Figure 10). This divergence as a function of color mirrors the same dichotomy seen at higher masses, where blue galaxies are preferentially diskier and red galaxies relatively thicker and spheroidal (see Figure 8). However, the outskirts of both red and blue dwarfs move towards more spheroidal shapes, suggestive of an in-situ formation mechanism for the extended stellar outskirts. This interpretation is also supported by a uniform trend towards more spheroidal outskirts in both field and satellite galaxies (see Figure 11).

The sample considered in this work is based on spectroscopic surveys; we are thus missing low surface brightness and ultra diffuse galaxies (UDGs). In particular, simulations suggest that the effective surface brightness cuts implemented in the SDSS and GAMA spectroscopic surveys bias dwarf samples towards more compact objects (Wright et al. 2020). Previous works have focused on samples of cluster UDGs: Burkert (2017) find that, for a sample of Coma UDGs, $\mu_B = \mu_C \sim 0.67$ (for a model with the assumption $C = B \leq A$). Similarly, Rong et al. (2019) find that for a triaxial model, $\mu_B = 0.86$ and $\mu_C = 0.49$. These results imply that cluster UDGs are typically rounder than high surface brightness dwarfs, with an intrinsic minor axis ratio (C/A) comparable to the outskirts of dwarfs in our sample.

However, samples of cluster UDGs are in highly overdense environments compared to the typical dwarf galaxy in our sample. To more fairly compare the structural composition of low surface brightness and high surface brightness dwarfs, and better understand the na-

ture of the relationship between these two populations, we must instead look to build a sufficiently large sample of UDGs in the field (e.g., Bellazzini et al. 2017; Leisman et al. 2017; Román & Trujillo 2017; Greco et al. 2018; Tanoglidis et al. 2020) such that the deprojection problem is tractable.

Our analysis also suggests that at $M_\star < 10^{8.5} M_\odot$, dwarfs become increasingly round (larger μ_C). However, our spectroscopic sample is far from mass-complete at $M_\star < 10^8 M_\odot$. In order to more comprehensively understand the properties of the dwarf population, it is necessary to construct a large and mass-complete sample of dwarfs at stellar masses lower than what is accessible with spectroscopic surveys currently in hand. As has been shown theoretically, star formation feedback is expected to play an increasingly dramatic role in the stellar structure of increasingly low mass dwarfs; extending the observational lever arm to lower stellar masses will provide an important constraint on prescriptions for star formation feedback, and provide novel insights into the stellar structure of such systems.

ACKNOWLEDGMENTS

The Hyper Suprime-Cam (HSC) collaboration includes the astronomical communities of Japan and Taiwan, and Princeton University. The HSC instrumentation and software were developed by the National Astronomical Observatory of Japan (NAOJ), the Kavli Institute for the Physics and Mathematics of the Universe (Kavli IPMU), the University of Tokyo, the High Energy Accelerator Research Organization (KEK), the Academia Sinica Institute for Astronomy and Astrophysics in Taiwan (ASIAA), and Princeton University. Funding was contributed by the FIRST program from the Japanese Cabinet Office, the Ministry of Education, Culture, Sports, Science and Technology (MEXT), the Japan Society for the Promotion of Science (JSPS), Japan Science and Technology Agency (JST), the Toray Science Foundation, NAOJ, Kavli IPMU, KEK, ASIAA, and Princeton University.

This paper makes use of software developed for the Large Synoptic Survey Telescope. We thank the LSST Project for making their code available as free software at <http://dm.lsst.org>

This paper is based [in part] on data collected at the Subaru Telescope and retrieved from the HSC data archive system, which is operated by Subaru Telescope and Astronomy Data Center (ADC) at NAOJ. Data analysis was in part carried out with the cooperation of Center for Computational Astrophysics (CfCA), NAOJ.

The Pan-STARRS1 Surveys (PS1) and the PS1 public science archive have been made possible through contributions by the Institute for Astronomy, the University of Hawaii, the Pan-STARRS Project Office, the Max Planck Society and its participating institutes, the Max Planck Institute for Astronomy, Heidelberg, and the Max Planck Institute for Extraterrestrial Physics, Garching, The Johns Hopkins University, Durham University, the University of Edinburgh, the Queens University Belfast, the Harvard-Smithsonian Center for Astrophysics, the Las Cumbres Observatory Global Telescope Network Incorporated, the National Central University of Taiwan, the Space Telescope Science Institute, the National Aeronautics and Space Administration under grant No. NNX08AR22G issued through the Planetary Science Division of the NASA Science Mission Directorate, the National Science Foundation grant No. AST-1238877, the University of Maryland, Eotvos Lorand University (ELTE), the Los Alamos National Laboratory, and the Gordon and Betty Moore Foundation.

GAMA is a joint European-Australasian project based around a spectroscopic campaign using the Anglo-Australian Telescope. The GAMA input catalogue is based on data taken from the Sloan Digital Sky Survey and the UKIRT Infrared Deep Sky Survey. Complementary imaging of the GAMA regions is being obtained by a number of independent survey programmes including GALEX MIS, VST KiDS, VISTA VIKING, WISE, Herschel-ATLAS, GMRT and ASKAP providing UV to radio coverage. GAMA is funded by the STFC (UK), the ARC (Australia), the AAO, and the participating institutions. The GAMA website is <http://www.gama-survey.org/>.

Funding for SDSS-III has been provided by the Alfred P. Sloan Foundation, the Participating Institutions, the National Science Foundation, and the U.S. Department of Energy Office of Science. The SDSS-III web site is <http://www.sdss3.org/>. SDSS-III is managed by the Astrophysical Research Consortium for the Participating Institutions of the SDSS-III Collaboration including the University of Arizona, the Brazilian Participation Group, Brookhaven National Laboratory, University of Cambridge, Carnegie Mellon University, University of Florida, the French Participation Group, the German Participation Group, Harvard University, the Instituto de Astrofísica de Canarias, the Michigan State/Notre Dame/JINA Participation Group, Johns Hopkins University, Lawrence Berkeley National Laboratory, Max Planck Institute for Astrophysics, Max Planck Institute for Extraterrestrial Physics, New Mexico State University, New York University, Ohio State University, Pennsylvania State University, University of Portsmouth,

Princeton University, the Spanish Participation Group, University of Tokyo, University of Utah, Vanderbilt University, University of Virginia, University of Washington, and Yale University.

Software: Astropy (Astropy Collaboration et al. 2013; Price-Whelan et al. 2018), matplotlib (Hunter 2007), SciPy (jon 2001), the IPython package (Pérez & Granger 2007), NumPy (Van Der Walt et al. 2011)

APPENDIX

A. TESTS OF THE BACKGROUND SUBTRACTION

The fidelity of the background subtraction is of key importance for two aspects of our analysis. First, background subtraction schemes that measure the sky background on scales comparable to the size of the target galaxies are liable to attribute diffuse light in the target outskirts to the sky background. This causes oversubtracted “dark rings” around galaxies that are large on the sky. Second, a uniform under- or oversubtraction of the background could affect our measurement of R_{eff} , as well as the estimate of our surface brightness limit.

Dark rings were a significant problem for nearby massive galaxies in the first data release of the HSC-SSP, prompting a change in the background estimation algorithm used for S18A (and the second data release). The updated algorithm is described in detail in Section 4.1 of Aihara et al. (2019); here we summarize the changes that most strongly affect performance for our sample.

The most pertinent change to the sky subtraction algorithm of S18A (or equivalently, PDR2) is that the sky is now estimated over the full focal plane, rather than over individual CCDs. In both cases, the sky is estimated by fitting a sixth-order two-dimensional Chebyshev polynomial to “superpixels”, which are themselves defined as the clipped mean of non-detection pixels within an $N \times N$ pixel grid. However, because the S18A pipeline fits a sky background over the entire focal plane of HSC, the superpixels can be much larger ($N = 1024$ pixels, $2'.8$ deg) than is possible with individual CCD sky estimation ($N = 256$ pixels, $43''$). The maximum radial range at which we measure the 1D surface brightness profiles in this work is 500 pixels ($84''$), significantly smaller than the S18A superpixels. Oversubtracted dark rings should thus not occur around our target galaxies in S18A – indeed, the galaxies are sufficiently small on the sky that the dark ring oversubtraction was not likely to be present even in the PDR1 pipeline.

To quantitatively test this statement, as well as to estimate the overall residual sky background in the vicinity of our targets, we follow the approach of Li et al. 2020, in prep., who test the performance of the surface brightness sensitivity and S18A background subtraction for a set of low- z ($z \sim 0.02$) and intermediate- z ($z \sim 0.40$) massive galaxies in HSC. From tests on mock galaxies and comparisons to imaging from the Dragonfly Wide Field Survey (Danieli et al. 2020) and the Dark Energy Camera Legacy Survey (DECaLS, Dey et al. 2019), they conclude that the intermediate-redshift massive galaxies are slightly uniformly undersubtracted, while the low-redshift massive galaxies are slightly uniformly oversubtracted. They moreover find that nearby ‘Sky Objects’ (SkyObj), can be used to estimate and correct for the residual over- or undersubtraction of the sky background to reach surface brightness sensitivities of $\mu_r \sim 29.5$ mag arcsec $^{-2}$. These Sky Objects are identified by the HSC data reduction pipeline (see Section 6.6.8 of Aihara et al. 2019) to be locations in which no objects are detected. Sky Object photometry is measured in apertures ranging from 20 arcsec to 118 arcsec in diameter.

We estimate the residual background around our dwarf sample by taking the mean flux in sky objects in the vicinity of our sample, as is done by Li et al. 2020, in prep for their more massive galaxy sample. We expect that the sky around our dwarf galaxies will be better estimated than the sky around the low- z massive galaxy for two reasons. First, our sample is characterized by nearly exponential profiles (Sérsic indices close to $n = 1$), meaning that their surface brightness profiles drop more steeply with distance than do the higher n massive galaxies in Li et al. 2020, in prep. Second, the massive galaxies are much more physically extended than our sample, and thus appear larger on-sky at fixed redshift.

Indeed, we find that the background around our galaxies tends to be slightly undersubtracted to a similar degree as the intermediate-redshift sample of Li et al. 2020, in prep. In Figure 13 we show the estimate of the sky background as a function of Sky Object aperture size for Sky Objects within 100 arcsec (green) and 200 arcsec (purple) of our target galaxies. For context, we reiterate that the maximum distance at which we measure profiles is 84 arcsec. We note that the two largest Sky Objects (of size 84 arcsec and 118 arcsec) are as large or larger than the extent over which we measure 1D profiles. Sky Objects with increasingly large apertures are more likely to include contributions from

background objects; The increase in the background level as a function of aperture size can be partially attributed to this effect. Regardless, we find that in all cases the additive background residual is $\lesssim 0.004$ counts per pixel. This corresponds to a change in surface brightness of $\lesssim 0.02$ mag arcsec $^{-2}$ for an object with surface brightness 28.5 mag arcsec $^{-2}$. The impact of the sky residual is small down to our nominal surface brightness limit of 28.5 mag arcsec $^{-2}$.

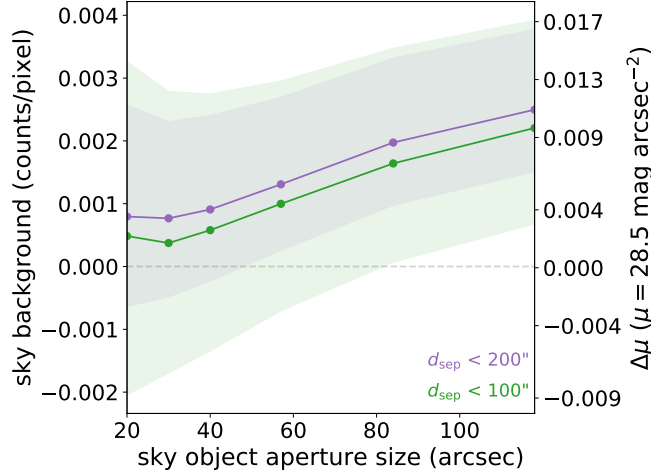


Figure 13. The residual sky in the HSC-i band near our sample as measured from nearby Sky Objects in the vicinity of our target galaxies. The sky background is measured as a function of Sky Object aperture size for Sky Objects within 100'' (green, 43149 Sky Objects) and 200'' (purple, 172974 Sky Objects) of our target galaxy sample. At left, we give the sky background in counts/pixel. At right, we show the change in surface brightness expected for an object with surface brightness 28.5 mag arcsec $^{-2}$. The solid curves show the median sky residual, while the shaded regions show the 25th and 75th percentiles. We find that the residual background has a negligible impact ($\lesssim 0.02$ mag arcsec $^{-2}$) on the surface brightness measured at our nominal surface brightness limit of 28.5 mag arcsec $^{-2}$.

B. MODEL SELECTION: ALLOWING FOR SHAPE-SIZE COVARIANCE

For a sample of galaxies at higher stellar mass and redshift, Zhang et al. (2019) showed that the inferred 3D shape distribution changes significantly when allowing a non-zero covariance between galaxy size and ellipticity.

To test whether this model is necessary for our sample of dwarfs, we fit a multivariate normal described by $\vec{\alpha} = \{\mu_A, \mu_B, \mu_C, \sigma_{AA}, \sigma_{BB}, \sigma_{CC}, \sigma_{AC}\}$ ⁶. As in Zhang et al. (2019), we only allow for a non-zero covariance between A and C . In order to understand whether the ($R_{\text{eff}}, b/a$) data demand a non-zero shape-size covariance, we initiate walkers normally distributed about the best-fit values inferred for the fiducial models. For each parameter X , initial values for the walkers are drawn from a normal distribution $\mathcal{N}(\tilde{X}, 0.25\tilde{X})$ where \tilde{X} is the best-fit value from the fiducial model.

The results of this test are shown in Figure 14. Though the data are well-described by a slightly negative shape-size covariance $\sigma_{AC} \sim -0.16$, we find that this model yields a small shift towards lower B/A , and a negligible shift in C/A . Therefore, because the model of (Zhang et al. 2019) adds three additional degrees of freedom to the model (μ_A, σ_A , and σ_{AC}), we choose to fit the marginalized b/a distribution, rather than ($R_{\text{eff}}, b/a$).

C. PARAMETER RECOVERY AND SAMPLE SIZE

As sample size decreases, the precision of our inferred model parameters $\vec{\alpha} = \{\mu_B, \mu_C, \sigma_B, \sigma_C\}$ decreases in kind. In Figure 15, we show the distribution of intrinsic axis ratios inferred for a sample of $N = \{100, 200, 1500, 2500\}$ galaxies. We find that at $N \sim 200$ galaxies, though μ_B and μ_C are well-recovered, σ_B and σ_C are increasingly overestimated⁷. We thus choose to only consider subsets of galaxies where $N > 700$.

⁶ here, A is in kpc, whereas B and C are defined as normalized lengths relative to A

⁷ We note that σ_B and σ_C are always overestimated when $\sigma_B = \sigma_C = 0$ due to the uncertainty in measuring 1D surface brightness profiles

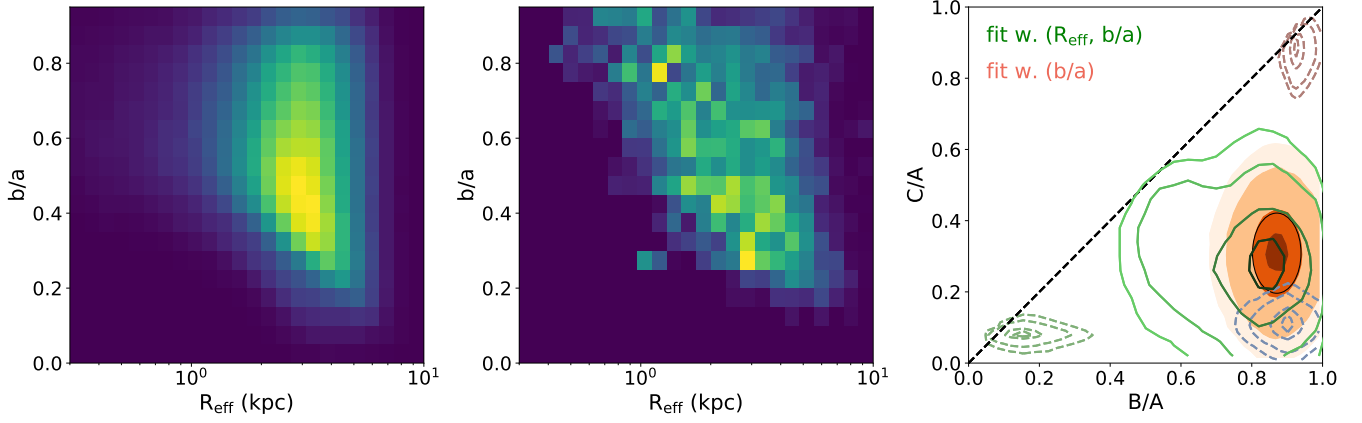


Figure 14. *Left:* the distribution of effective radius and projected axis ratio for a sample drawn from the posterior distribution for a model where we allow for a non-zero covariance between C/A and R_{eff} . *Middle:* the distribution over R_{eff} and projected axis ratio (b/a) for the observed galaxies. *Right:* the inferred distribution over intrinsic axis ratios for the fiducial model (orange filled contours) and the model at left (green unfilled contours).

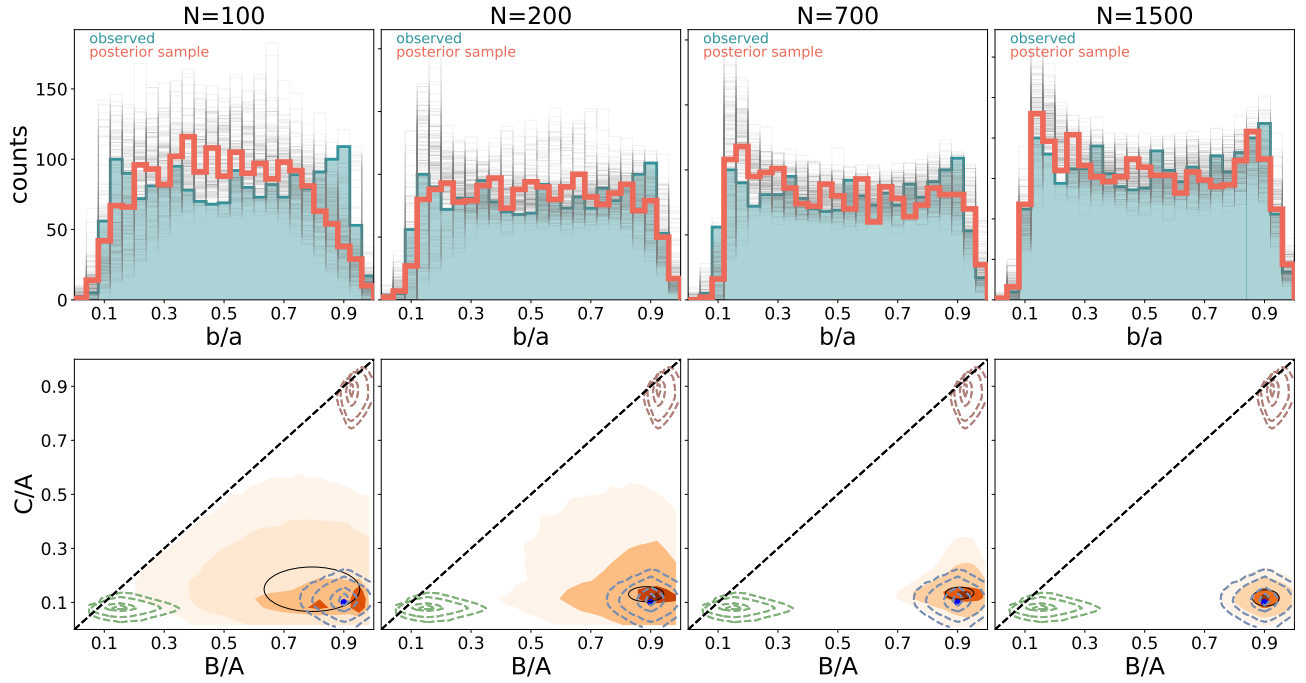


Figure 15. For a population of mock disk galaxies described by $\vec{\alpha} = \{\mu_B, \mu_C, \sigma_B, \sigma_C\} = \{0.9, 0.1, 0., 0.\}$, we investigate the precision at which the model parameters $\vec{\alpha}$ may be recovered as a function of sample size N . The top row shows, in each panel, the true distribution of the projected axis ratio b/a in teal and the posterior sample in orange. Individual draws from the posterior are shown in grey. The bottom row shows the distribution of intrinsic axis ratios (B/A and C/A) from the posterior sample in orange. The maximum a posteriori estimate is shown by the black ellipse. The pure disk, prolate, and spheroidal populations are shown by dashed contours (see Figure 7). A successful recovery is one in which the orange contours of the posterior samples coincides with the dashed blue contours of the pure disk population.

REFERENCES

2001, SciPy: Open source scientific tools for Python

Abadi, M. G., Navarro, J. F., & Steinmetz, M. 2006,
MNRAS, 365, 747

- Abazajian, K., Adelman-McCarthy, J. K., Agüeros, M. A., et al. 2004, *AJ*, **128**, 502
- Ahumada, R., Allende Prieto, C., Almeida, A., et al. 2019, arXiv e-prints, arXiv:1912.02905
- Aihara, H., Armstrong, R., Bickerton, S., et al. 2018a, *PASJ*, **70**, S8
- Aihara, H., Arimoto, N., Armstrong, R., et al. 2018b, *PASJ*, **70**, S4
- Aihara, H., AlSayyad, Y., Ando, M., et al. 2019, *PASJ*, **71**, 114
- Amorisco, N. C. 2017, *MNRAS*, **464**, 2882
- Ann, H. B. 2017, *Journal of Korean Astronomical Society*, **50**, 111
- Aparicio, A., & Tikhonov, N. 2000, *AJ*, **119**, 2183
- Aparicio, A., Tikhonov, N., & Karachentsev, I. 2000, *AJ*, **119**, 177
- Astropy Collaboration, Robitaille, T. P., Tollerud, E. J., et al. 2013, *A&A*, **558**, A33
- Baldry, I. K., Driver, S. P., Loveday, J., et al. 2012, *MNRAS*, **421**, 621
- Bekki, K. 2008, *ApJL*, **680**, L29
- Bellazzini, M., Belokurov, V., Magrini, L., et al. 2017, *MNRAS*, **467**, 3751
- Bernard, E. J., Aparicio, A., Gallart, C., Padilla-Torres, C. P., & Panniello, M. 2007, *AJ*, **134**, 1124
- Besla, G., Patton, D. R., Stierwalt, S., et al. 2018, *MNRAS*, **480**, 3376
- Binney, J., & Tremaine, S. 2008, *Galactic Dynamics: Second Edition*
- Blanton, M. R., Kazin, E., Muna, D., Weaver, B. A., & Price-Whelan, A. 2011, *AJ*, **142**, 31
- Bosch, J., Armstrong, R., Bickerton, S., et al. 2018, *PASJ*, **70**, S5
- Brook, C. B., Di Cintio, A., Knebe, A., et al. 2014, *ApJL*, **784**, L14
- Bullock, J. S., & Johnston, K. V. 2005, *ApJ*, **635**, 931
- Burkert, A. 2017, *ApJ*, **838**, 93
- Chabrier, G. 2003, *ApJL*, **586**, L133
- Compère, P., López-Corredoira, M., & Garzón, F. 2014, *A&A*, **571**, A98
- Conroy, C., Gunn, J. E., & White, M. 2009, *ApJ*, **699**, 486
- Coupon, J., Czakon, N., Bosch, J., et al. 2018, *PASJ*, **70**, S7
- Danieli, S., Lokhorst, D., Zhang, J., et al. 2020, *ApJ*, **894**, 119
- Dashyan, G., & Dubois, Y. 2020, arXiv e-prints, arXiv:2003.09900
- Dawson, K. S., Schlegel, D. J., Ahn, C. P., et al. 2013, *AJ*, **145**, 10
- Deason, A., Wetzel, A., & Garrison-Kimmel, S. 2014, *ApJ*, **794**, 115
- Demers, S., Battinelli, P., & Artigau, E. 2006, *A&A*, **456**, 905
- Dey, A., Schlegel, D. J., Lang, D., et al. 2019, *AJ*, **157**, 168
- Doi, M., Tanaka, M., Fukugita, M., et al. 2010, *AJ*, **139**, 1628
- Dressler, A. 1980, *ApJ*, **236**, 351
- El-Badry, K., Wetzel, A., Geha, M., et al. 2016, *ApJ*, **820**, 131
- Foreman-Mackey, D., Hogg, D. W., Lang, D., & Goodman, J. 2013, *PASP*, **125**, 306
- Furusawa, H., Koike, M., Takata, T., et al. 2018, *PASJ*, **70**, S3
- Geha, M., Blanton, M. R., Yan, R., & Tinker, J. L. 2012, *ApJ*, **757**, 85
- Grebel, E. K. 1999, in *IAU Symposium*, Vol. 192, *The Stellar Content of Local Group Galaxies*, ed. P. Whitelock & R. Cannon, 17
- Greco, J. P., Goulding, A. D., Greene, J. E., et al. 2018, *ApJ*, **866**, 112
- Hargis, J. R., Albers, S., Crnojević, D., et al. 2020, *ApJ*, **888**, 31
- Hidalgo, S. L., Marín-Franch, A., & Aparicio, A. 2003, *AJ*, **125**, 1247
- Hu, C.-Y. 2019, *MNRAS*, **483**, 3363
- Huang, S., Leauthaud, A., Greene, J. E., et al. 2018a, *MNRAS*, **475**, 3348
- Huang, S., Leauthaud, A., Murata, R., et al. 2018b, *PASJ*, **70**, S6
- Hunter, J. D. 2007, *Computing in Science & Engineering*, **9**, 90
- Iorio, G., & Belokurov, V. 2019, *MNRAS*, **482**, 3868
- Jedrzejewski, R. I. 1987, *MNRAS*, **226**, 747
- Kado-Fong, E., Greene, J. E., Greco, J. P., et al. 2020, *AJ*, **159**, 103
- Kawanomoto, S., Uruguchi, F., Komiyama, Y., et al. 2018, *PASJ*, **70**, 66
- Knapen, J. H., & Trujillo, I. 2017, *Ultra-Deep Imaging: Structure of Disks and Haloes*, ed. J. H. Knapen, J. C. Lee, & A. Gil de Paz (Cham: Springer International Publishing), 255
- Komiyama, Y., Obuchi, Y., Nakaya, H., et al. 2018, *PASJ*, **70**, S2
- Kormendy, J., & Bender, R. 2012, *ApJS*, **198**, 2
- Kroupa, P. 2001, *MNRAS*, **322**, 231
- Leisman, L., Haynes, M. P., Janowiecki, S., et al. 2017, *ApJ*, **842**, 133
- Lin, D. N. C., & Faber, S. M. 1983, *ApJL*, **266**, L21
- Liske, J., Baldry, I. K., Driver, S. P., et al. 2015, *MNRAS*, **452**, 2087

- Maxwell, A. J., Wadsley, J., Couchman, H. M. P., & Mashchenko, S. 2012, *ApJL*, **755**, L35
- Méndez-Abreu, J., Costantin, L., Aguerri, J. A. L., de Lorenzo-Cáceres, A., & Corsini, E. M. 2018, *MNRAS*, **479**, 4172
- Minniti, D., & Zijlstra, A. A. 1996, *ApJL*, **467**, L13
- Minniti, D., Zijlstra, A. A., & Alonso, M. V. 1999, *AJ*, **117**, 881
- Miyazaki, S., Komiyama, Y., Kawanomoto, S., et al. 2018, *PASJ*, **70**, S1
- Moster, B. P., Naab, T., & White, S. D. M. 2013, *MNRAS*, **428**, 3121
- Nidever, D. L., Olsen, K., Choi, Y., et al. 2019a, *ApJ*, **874**, 118
- . 2019b, *ApJ*, **874**, 118
- Padilla, N. D., & Strauss, M. A. 2008, *MNRAS*, **388**, 1321
- Panther, B., Jimenez, R., Heavens, A. F., & Charlot, S. 2007, *MNRAS*, **378**, 1550
- Pérez, F., & Granger, B. E. 2007, *Computing in Science and Engineering*, **9**, 21
- Pillepich, A., Nelson, D., Springel, V., et al. 2019, *MNRAS*, **490**, 3196
- Postman, M., & Geller, M. J. 1984, *ApJ*, **281**, 95
- Price-Whelan, A. M., Sipőcz, B. M., Günther, H. M., et al. 2018, *AJ*, **156**, 123
- Pucha, R., Carlin, J. L., Willman, B., et al. 2019, *ApJ*, **880**, 104
- Purcell, C. W., Bullock, J. S., & Zentner, A. R. 2007, *ApJ*, **666**, 20
- Putko, J., Sánchez Almeida, J., Muñoz-Tuñón, C., et al. 2019, *ApJ*, **883**, 10
- Reid, B., Ho, S., Padmanabhan, N., et al. 2016, *MNRAS*, **455**, 1553
- Rodríguez, S., Padilla, N. D., & García Lambas, D. 2016, *MNRAS*, **456**, 571
- Román, J., & Trujillo, I. 2017, *MNRAS*, **468**, 4039
- Rong, Y., Dong, X.-Y., Puzia, T. H., et al. 2019, arXiv e-prints, arXiv:1907.10079
- Roychowdhury, S., Chengalur, J. N., Karachentsev, I. D., & Kaisina, E. I. 2013, *MNRAS*, **436**, L104
- Sánchez-Janssen, R., Méndez-Abreu, J., & Aguerri, J. A. L. 2010, *MNRAS*, **406**, L65
- Schönrich, R., & Binney, J. 2009, *MNRAS*, **399**, 1145
- Simonneau, E., Varela, A. M., & Muñoz-Tunon, C. 1998, *Nuovo Cimento B Serie*, **113B**, 927
- Stinson, G. S., Dalcanton, J. J., Quinn, T., et al. 2009, *MNRAS*, **395**, 1455
- Strader, J., Seth, A. C., & Caldwell, N. 2012, *AJ*, **143**, 52
- Strauss, M. A., Weinberg, D. H., Lupton, R. H., et al. 2002, *AJ*, **124**, 1810
- Tanoglidis, D., Drlica-Wagner, A., Wei, K., et al. 2020, arXiv e-prints, arXiv:2006.04294
- Taylor, E. N., Hopkins, A. M., Baldry, I. K., et al. 2011, *MNRAS*, **418**, 1587
- Trujillo, I., & Fliri, J. 2016, *ApJ*, **823**, 123
- Van Der Walt, S., Colbert, S. C., & Varoquaux, G. 2011, *Computing in Science & Engineering*, **13**, 22
- van der Wel, A., Chang, Y.-Y., Bell, E. F., et al. 2014, *ApJL*, **792**, L6
- Wang, W., Han, J., Sonnenfeld, A., et al. 2019, *MNRAS*, **487**, 1580
- Weinmann, S. M., van den Bosch, F. C., Yang, X., & Mo, H. J. 2006, *MNRAS*, **366**, 2
- Wheeler, C., Pace, A. B., Bullock, J. S., et al. 2017, *MNRAS*, **465**, 2420
- Wright, A. C., Tremmel, M., Brooks, A. M., et al. 2020, arXiv e-prints, arXiv:2005.07634
- Wright, A. H., Robotham, A. S. G., Driver, S. P., et al. 2017, *MNRAS*, **470**, 283
- Zaritsky, D., Harris, J., Grebel, E. K., & Thompson, I. B. 2000, *ApJL*, **534**, L53
- Zhang, H., Primack, J. R., Faber, S. M., et al. 2019, *MNRAS*, **484**, 5170